Title

Aridification of Northwest Australia and Nutrient Decline in the Timor Sea During the 40 Kyr World

Journal

Paleoceanography and Paleoclimatology, 38(10)

ISSN

2572-4517

Authors

Zhang, Y

Andrade, T

Ravelo, AC

et al.

Publication Date

2023-10-01

DOI

10.1029/2023pa004683

Paleoceanography and Paleoclimatology

AGU ADVANCING EARTH AND SPACE SCIENCES

RESEARCH ARTICLE
10.1029/2023PA004683

Aridification of Northwest Australia and Nutrient Decline in the Timor Sea During the 40 Kyr World

Y. Zhang[1], T. Andrade[1,2], A. C. Ravelo[1], L. Gong[3], A. Holbourn[3], G. Connock[4,5], X. L. Liu[4], and I. W. Aiello[6]

[1]Department of Ocean Sciences, University of California, Santa Cruz, CA, USA, [2]Blue Planet Systems, Los Gatos, CA, USA, [3]Institute of Geosciences, Christian-Albrechts-University, Kiel, Germany, [4]School of Geosciences, University of Oklahoma, Norman, OK, USA, [5]U.S. Geological Survey, Richmond, VA, USA, [6]Moss Landing Marine Laboratories, San Jose State University, Moss Landing, CA, USA

Key Points:

- Northwest Australia underwent aridification from ~1,700 to 1,400 ka due to restricted Indonesian Throughflow and warm pool contraction
- Decreased productivity in the Timor Sea from ~1,700 to 1,400 ka reflected decreased nutrient supply from Pacific source water
- Orbital variation in productivity and terrigenous input in the Timor Sea during the 40 kyr world are driven by multiple mechanisms

Supporting Information:

Supporting Information may be found in the online version of this article.

Correspondence to:

Y. Zhang,
yzhan543@ucsc.edu

Citation:

Zhang, Y., Andrade, T., Ravelo, A. C., Gong, L., Holbourn, A., Connock, G., et al. (2023). Aridification of northwest Australia and nutrient decline in the Timor Sea during the 40 kyr world. *Paleoceanography and Paleoclimatology*, *38*, e2023PA004683. https://doi.org/10.1029/2023PA004683

Received 20 JUN 2023
Accepted 8 SEP 2023

Author Contributions:

Conceptualization: Y. Zhang, A. C. Ravelo, A. Holbourn, G. Connock, X. L. Liu, I. W. Aiello
Data curation: Y. Zhang, T. Andrade, L. Gong, A. Holbourn, G. Connock, X. L. Liu
Formal analysis: Y. Zhang, T. Andrade, A. C. Ravelo, L. Gong, A. Holbourn, G. Connock, X. L. Liu
Funding acquisition: Y. Zhang, A. C. Ravelo

Abstract Studying tropical hydroclimate and productivity change in the past is critical for understanding global climate dynamics. Northwest Australia is an ideal location for investigating Australian monsoon dynamics, the variability of the Indonesian Throughflow (ITF), and their impact on past productivity and Pacific warm pool evolution, which remain poorly understood during the 40 kyr world in the mid-early Pleistocene. In this study, we present multi-proxy records from International Ocean Discovery Program (IODP) Site U1483 in the Timor Sea spanning the last 2,000 ka, including orbitally-resolved records from the 40 kyr world between 2,000 and 1,300 ka. Our results suggest that northwest Australia underwent a step of increased aridification and that productivity in the Timor Sea declined during the transition from ~1,700 to ~1,400 ka. We attribute this aridification to the reduced moisture supply to this region caused by the ITF restriction and warm pool contraction. We ascribe the declined productivity to a decrease in the nutrient supply of the Pacific source water associated with global nutrient redistribution. At orbital timescale, multiple mechanisms, including sea level changes, monsoon, and the Intertropical Convergence Zone (ITCZ) dynamics, and variations in the ITF and Walker circulation could have controlled variations of productivity and terrigenous input in the Timor Sea during the 40 kyr world. Our bulk nitrogen and benthic carbon isotope records suggest a strong coupling to biogeochemical changes in the Pacific during this period. This research contributes to a better understanding of tropical hydroclimate and productivity changes during the 40 kyr world.

Plain Language Summary The northwest Australian region is located at the southwestern edge of the Indo-Pacific Warm Pool and experiences a seasonal monsoon climate. Oceanic and climate conditions in this region are also strongly influenced by the Indonesian Throughflow (ITF), which is the only tropical pathway in the modern ocean connecting the Pacific and Indian Oceans and providing the main conduit for the exchange of water, salt, and heat between these oceans. These conditions make northwest Australia a strategic location to explore Australian monsoon dynamics, the variability of the ITF, and the interaction between tropical hydroclimate and productivity in the past. However, these processes are poorly documented during the 40 kyr world in the mid-early Pleistocene, when glacial-interglacial cycles mainly varied at the 41 kyr obliquity band. Here, we present multiple-proxy marine records from a site directly impacted by the ITF and we examine terrigenous input and productivity changes in this region over the last 2,000 kyr. Our results suggest that northwest Australia underwent a step of increased aridification and that productivity in the Timor Sea declined during the transition from ~1,700 to ~1,400 ka, due to restriction of the ITF, warm pool contraction, and decreased nutrient supply from the Pacific source water.

1. Introduction

Studying past changes in tropical hydroclimate and productivity is recognized as important for understanding global climate dynamics. The northwest Australian region, located at the southern border of the Indo-Pacific Warm Pool (IPWP), is strongly influenced by the trans-equatorial Indonesian Throughflow (ITF) and the seasonal reversal of monsoonal wind and precipitation. It is an ideal location for investigating the variability of the ITF, Australian monsoon dynamics, and their impact on past productivity and IPWP evolution (Beaufort et al., 2010; De Deckker et al., 2014; Holbourn et al., 2005; Müller & Opdyke, 2000). Hydroclimate and productivity changes in the northwest Australian region are influenced by complex, interacting mechanisms. Not only does the Australian monsoon and the seasonal migration of the rain belt (the Intertropical Convergence Zone (ITCZ)) play a

Investigation: Y. Zhang, T. Andrade, A. C. Ravelo, A. Holbourn, G. Connock, X. L. Liu
Methodology: Y. Zhang, T. Andrade, A. C. Ravelo, L. Gong, A. Holbourn, G. Connock, X. L. Liu
Project Administration: A. C. Ravelo
Resources: Y. Zhang, A. C. Ravelo, A. Holbourn, G. Connock, I. W. Aiello
Software: Y. Zhang, L. Gong
Supervision: A. C. Ravelo
Validation: Y. Zhang, A. C. Ravelo, A. Holbourn, G. Connock, X. L. Liu
Visualization: Y. Zhang
Writing – original draft: Y. Zhang, A. C. Ravelo
Writing – review & editing: Y. Zhang, T. Andrade, A. C. Ravelo, L. Gong, A. Holbourn, G. Connock, X. L. Liu, I. W. Aiello

prominent role in controlling precipitation and productivity patterns, but this region is also influenced by the tropical ocean zonal thermal circulation (e.g., Walker circulation), and the regional moisture and nutrient supply regulated by factors such as the intensity of the ITF (Beck et al., 2018). Therefore, reconstructions of the terrigenous discharge and productivity variations have the potential to track and elucidate the processes responsible for climatic and oceanographic changes in the northwest Australian region.

Global climate has experienced a major transition in the periodicity of the glacial-interglacial cycles from 41 kyr (40 kyr world) to quasi-100 kyr (100 kyr world) during the mid-Pleistocene (Lisiecki & Raymo, 2005; Pisias & Moore, 1981). The vast majority of previous studies on past climate change over the northwest Australian region focused on the Holocene and late Pleistocene (Auer et al., 2019; Beaufort et al., 2010; De Deckker et al., 2014; Holbourn et al., 2005; Ishiwa et al., 2019; Kuhnt et al., 2015; Müller & Opdyke, 2000; Stuut et al., 2014). These studies indicated that insolation forcing and sea level changes have played critical roles in controlling monsoon activity and local productivity in this region during the 100 kyr world (Beaufort et al., 2010; Holbourn et al., 2005; Müller & Opdyke, 2000; Stuut et al., 2014). Several recent reconstructions of sea surface temperature (SST) and terrigenous input along the northwest Australian margin focusing on sediments recovered by International Ocean Discovery Program (IODP) Expedition 356 have offered valuable insight into past ITF and Leeuwin Current variability and the impact on Pliocene and Pleistocene climate (Christensen et al., 2017; He et al., 2021; Petrick et al., 2019; Smith et al., 2020; Stuut et al., 2019). These studies proposed that during the Plio-Pleistocene, increasing near-shore aridity in northwest Australia was largely driven by the progressive constriction of the ITF, resulting in lower SSTs and reduced moisture supply to this region. However, there are few orbitally-resolved reconstructions that directly reflect ITF variability, past productivity changes, and Australian monsoon dynamics during the 40 kyr world in the mid-early Pleistocene (Chen et al., 2022; Zhang et al., 2020).

The Timor Sea is located along the main outflow route of the ITF and is therefore strongly influenced by ITF variability and sea level changes. Through regulating the fresh and warm water transport from the Pacific to the Indian Oceans, ITF dynamics interact with monsoon systems and affect the upper ocean thermal structure (Feng et al., 2018) and local productivity of the Timor Sea (Müller & Opdyke, 2000). Holbourn et al. (2005) found that productivity fluctuations in the Timor Sea were strongly influenced by monsoonal wind patterns and were also modulated by sea level–related variations in the intensity of the ITF in the 100 kyr world of the late Pleistocene. Zhang et al. (2020) pointed out that terrigenous/monsoonal discharge in the Timor Sea was linked to Indo-Pacific ITCZ dynamics over the last 410 kyr. In the 100 kyr world, precessional variability in both sea level changes and insolation forcing makes it complicated to differentiate the main driving force of monsoon dynamics and productivity change. However, in the 40 kyr world, sea level and global climate changes are strongly dominated by 41 kyr variability (obliquity band), whereas local insolation forcing is dominated by 19–23 kyr variability (precession band). Thus, extending those records to the 40 kyr world will help us disentangle the mechanisms that drive changes in the Australian monsoon, hydroclimate, and productivity in this region.

Site U1483, drilled during IODP Expedition 363, is located in the Timor Sea within the main ITF outflow (Figure 1a) and thus offers a unique opportunity to investigate ITF dynamics, variations in productivity, and Australian monsoon variability (Figure 1b) (Beck et al., 2018). In this study, using multi-proxy marine records spanning the last 2,000 kyr at Site U1483, including orbitally-resolved records from the 40 kyr world between 2,000 and 1,300 ka, we examine terrigenous input and productivity changes in this region. First, our results suggest that northwest Australia underwent a step of increased aridification and that productivity in the Timor Sea declined from ~1,700 to ~1,400 ka, and we discuss possible mechanisms for this transition. Second, our high-resolution proxy records from 2,000 to 1,300 ka show orbital variability and we explore the mechanisms that could have driven this variability. Finally, our bulk nitrogen and benthic carbon isotope records suggest a strong coupling to biogeochemical changes in the Pacific Ocean.

2. Oceanographic and Climatic Setting at Site U1483

Site U1483 was drilled during International Ocean Discovery Program (IODP) Expedition 363 in the IPWP. Site U1483 (13°50.24′S, 121°48.25′E, water depth of 1,733 m) is located on the Scott Plateau in the Timor Sea in the northeast Indian Ocean off the northwest Australian coast (Figure 1a), close to Site MD01-2378 (13° 04.95′S, 121°47.27′E, water depth of 1,783 m) (Holbourn et al., 2005). Site U1483 is located at the southwestern edge of the modern IPWP, beneath the path of the main ITF outflow through the Timor Strait (sill depth of 1,500 m) (Figures 1a and 1c), which is the second largest magnitude component of the ITF in the modern ocean and contributes to the shallow water conditions along the northwest Australian coast (Kuhnt et al., 2004). The ITF

10.1029/2023PA004683

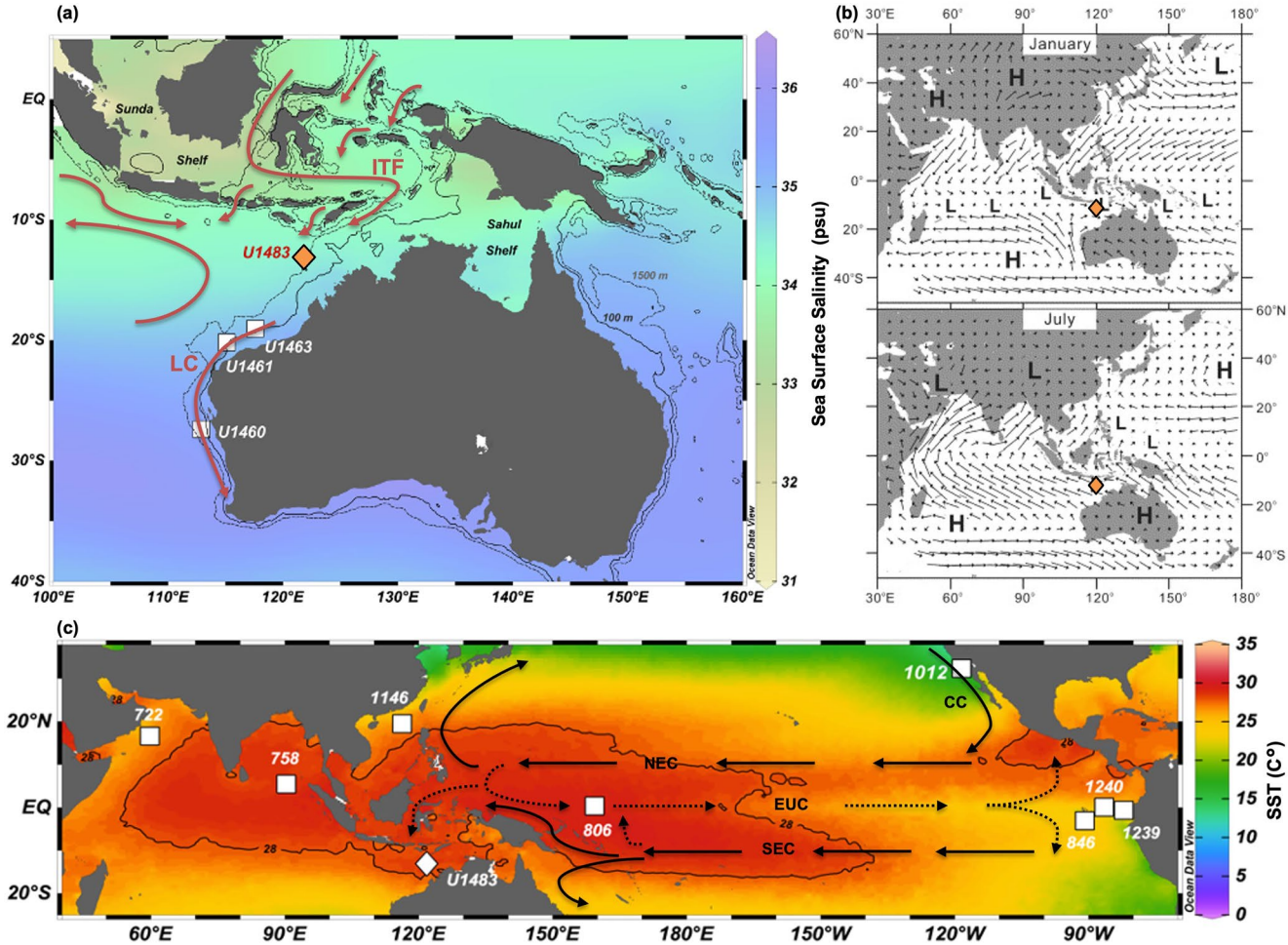

Figure 1. Study Site U1483 (denoted by the diamond) shown on (a) the map of annual sea surface salinity with regional west Indo-Pacific currents in modern ocean (modified from Gallagher et al. (2009)); (b) on the map of modern Asian-Australian monsoon system (modified from Wang et al. (2005)) and (c) on the map of annual sea surface temperature in tropical Indo-Pacific region (modified from Rousselle et al. (2013)). Other sites mentioned in this study are denoted by a square. Panel (b) shows pressure and surface wind pattern in boreal winter (right top panel) and in boreal summer (right bottom panel). Average annual surface temperature and surface salinity from the World Ocean Atlas 2018 (Boyer et al., 2018) plotted using Ocean Data View (ODV) (Schlitzer, 2023). ITF = Indonesian throughflow; LC = Leeuwin Current; NEC = North Equatorial Current; SEC = South Equatorial Current; EUC = Equatorial Undercurrent; CC = California Current.

brings warm, fresh, and oligotrophic water from the Pacific to the Indian Ocean and affects the upper ocean mixing in the Timor Sea (Feng et al., 2018). Today, hydrographic conditions at Site U1483 are clearly dominated by the ITF outflow of warm, low-salinity surface water.

In the modern ocean, the ITF geostrophic transport is strongest in austral winter (Gordon et al., 2003) and is modified by the El Niño-Southern Oscillation (ENSO) through the influence of the Pacific waveguide (Feng et al., 2018, Figures 1a and 1b). The upper waters of the ITF in the Timor Sea (<1,000 m) mostly originate from the subtropical North Pacific surface waters and the North Pacific Intermediate Water, flowing through the Mindanao Current (Gordon & Fine, 1996; Talley & Sprintall, 2005). The intermediate water in the Timor Sea (1,000–1,500 m) is derived from the Antarctic Intermediate Water (AAIW) from the South Pacific via the Halmahera Sea and the deep part of the Indonesian intermediate water (Chen et al., 2022; Tomczak & Godfrey, 1994). The deep water in the Timor Sea is sourced from the Indian Deep water (Tomczak & Godfrey, 1994). The Timor strait has an average depth of around 300 m and since sea level ranged from −100 to +25 m during the mid-early Pleistocene (1,300–2,000 ka) (Rohling et al., 2014), thus there was continuous flow through the Timor passage during the time interval we studied (Figure 1a).

Northwest Australia experiences monsoon winds, which are directly driven by the temperature and pressure gradient between the land mass and the nearby upper ocean (Suppiah, 1992) (Figure 1b). During the austral

summer, due to the low pressure over the Pilbara in northwest Australia, where local insolation heats the land, wind originating from the north-west as a part of south Asian monsoon, brings moisture from the Indian Ocean to northwest Australia, leading to high precipitation and increased riverine sediment load into the ocean (Chang et al., 2006; Suppiah, 1992). During the austral winter, the strong south-east trade winds blow offshore (contributing to the south Asian summer monsoon), resulting in intensified costal upwelling and dry conditions in northwest Australia. Australian monsoon could also be considered as arising from the seasonal migration of the Indo-Pacific ITCZ associated with the tropical overturning (Hadley) circulation changes (Geen et al., 2020; Heidemann et al., 2023), resulting in a distinct seasonal variability in precipitation. Furthermore, northwest Australia is situated to the south of the Maritime continent and borders the IPWP. The precipitation in this region is also affected by the Walker circulation, which is influenced by sea-level modulated land exposure and tropical Pacific dynamics (DiNezio et al., 2016; Heidemann et al., 2023). Thus, reconstructions of terrigenous input and paleo-productivity changes can potentially track past Australian monsoon dynamics and hydroclimate changes over northwest Australia.

3. Materials and Methods

3.1. Site U1483 Sedimentology and Bulk Measurements

Cores from Site U1483 contain clay-rich and clay-foraminifera-rich nannofossil ooze (Rosenthal et al., 2017). Our samples are taken from 0.44 to 199.53 m core composite depth below seafloor (CCSF), which is above the first appearance of soft sediment deformation. We sampled every 150 cm to achieve an average ~15 kyr resolution spanning from ~2,000 to 0 ka and every 30 cm to achieve an average ~3 kyr resolution between 127.05 and 199.53 m CCSF spanning from ~2,000 to ~1,300 ka. Bulk nitrogen isotope ($\delta^{15}N$) and total nitrogen (TN, wt%) were analyzed from these samples (methods see Text S1 in Supporting Information S1). A subset of the samples spanning from ~2,000 to 0 ka with an average ~22 ka resolution were analyzed for carbon isotope of total organic carbon (TOC) ($\delta^{13}C_{org}$) to distinguish the terrestrial and marine sourced organic matter (methods see Text S2 in Supporting Information S1). TOC:TN ratios are calculated to help assess inorganic N contamination. All bulk sediment measurements were analyzed on the Carlo Erba 1,108 elemental analyzer (interfaced to a Thermo Finningan Delta Plus XP IRMS) at the University of California, Santa Cruz. The external precision is ±0.20 ‰ for $\delta^{15}N$, ±0.10 wt% for TN wt%, ±0.10‰ for $\delta^{13}C_{org}$ and ±0.10 for TOC:TN ratios. We obtained $CaCO_3$ wt% using three methods (Text S3, Figures S1 and S2 in Supporting Information S1). Specifically, $CaCO_3$ $wt\%_{EA}$ were calculated using $CaCO_3 wt\% = \frac{(\mu gC) - (6 \cdot \mu gN)}{\text{sample mass}}$, under the assumption that TOC:TN ratio is equivalent to 7. Our results confirm that the estimations of $CaCO_3$ $wt\%_{EA}$ are accurate and thus we use $CaCO_3$ $wt\%_{EA}$ values for all the paleoceanographic interpretations hereafter in this paper.

3.2. Benthic Foraminiferal Stable Isotope Analysis and Age Model

Benthic foraminiferal stable isotope measurements (from 1,922 to 1,589 ka) were conducted at the Institute of Geosciences, Christian-Albrechts-University, Kiel (Germany). Detailed methods are provided in Gong et al. (2023). The analysis was carried out on the benthic foraminifers *Cibicidoides wuellerstorfi and/or Cibicidoides mundulus* from the size fraction >250 μm. *Uvigerina* spp. were measured when *C. wuellerstorfi* and *C. mundulus* were rare or absent (Zhang et al., 2023). The external standard error is better than ±0.08‰ for $\delta^{18}O$ and ±0.05‰ for $\delta^{13}C$ based on international standards.

From 1,922 to 0 ka, our age model is based on the correlation of benthic foraminiferal $\delta^{18}O$ to the LR04 stack (Lisiecki & Raymo, 2005). We use the published age model from Zhang et al. (2020) (420–0 ka) and from Gong et al. (2023) (1,587–420 ka), and in this study extend the age model from 1,922 to 1,587 ka (Figure S3 in Supporting Information S1). The interval between 1,922 and 1,587 ka has been tuned to the LR04 stack and the interval between 1,587 and 0 ka is based on previous reported age-models. From 2,000 to 1,922 ka, our age model is generated by correlating XRF-derived high-resolution records of Log (Mn/S) (see Section 3.3) from Site U1483 and the LR04 stack using QAnalySeries (Kotov & Pälike, 2018) using five tie points (Figure S4 in Supporting Information S1). Mass-based accumulation rates (MAR) are calculated based on the sedimentation rates and dry bulk density (DBD) values (Figure S5 in Supporting Information S1).

3.3. Organic Geochemistry

A set of 32 sediment samples was selected for lipid biomarker analysis using a recently developed reverse phase liquid chromatography quadrupole time-of-flight mass spectrometry method with electrospray ionization

(RPLC-ESI-qTOF-MS) (Liao et al., 2023) and were measured at University of Oklahoma. This new analytical approach exhibits greater sensitivity in detecting the low-concentration tri-unsaturated alkenones compared to conventional gas chromatography-flame ionization detector (GC-FID) analyses, therefore the tri-unsaturated C_{37} alkenones were distinctly detected in all analyzed samples of this study. Sample preparation and instrument setup followed method published in Connock et al. (2022). The Prahl and Wakeham (1987) calibration was applied to the $U^{K'}_{37}$—based SST, which exhibits same features and trend as using Müller et al. (1998) calibration (Zhang et al., 2023). The Schouten et al. (2002) calibration was applied to the TEX_{86}—based SST record. The Branched versus Isoprenoid Tetraether (BIT) index was calculated following Hopmans et al. (2004), as an indication of soil inputs (thus terrigenous input) of glycerol dialkyl glycerol tetraether (GDGT) (Hopmans et al., 2004).

3.4. X-Ray Fluorescence Core Scanning and Other Analyses

We performed high-resolution X-ray fluorescence (XRF) core scanning with the second Generation Avaatech XRF Core Scanner at the Institute of Geosciences, Christian-Albrechts-University, Kiel (Germany). The archive halves were equilibrated to room temperature before scanning and a thin layer of sediment was removed from the top to obtain a fresh, even surface for scanning. We scanned at 2 cm intervals along the shipboard splice with approximately 1–2 m overlaps at splice tie points. Scanning was performed with 10 kV (750 μA, 10s acquisition time, no filter) and 30 kV (2,000 μA, 20s acquisition time, Pd-thick filter) on the archive halves, which were covered with a 4 μm thick Chemplex Prolene Thin-Film foil to prevent contamination of the XRF detector. We used a crosscore slit size of 1.2 cm and a downcore slit size of 1 cm. The data reported here were acquired by a XR-100CR detector from Amptek and an Oxford Instruments 50W XTF5011 X-Ray tube with rhodium (Rh) target material. Raw X-ray spectra were converted into area counts using the iterative least-square software package WIN_AXIL from Canberra Eurisys and a core-specific model. The elements Al, Si, S, K, Ca, Ti, Mn, and Fe were analyzed with the 10-kV setting. Measured area counts per second of the spectral peaks of each element were transferred to logarithmic elemental ratios, which provide the most easily interpretable signals of relative changes in chemical composition. The use of elemental ratios minimizes the risk of measurement artifacts from variable signal intensities due to changes in sediment density, pore volume, water content and matrix effects.

We obtained the in-situ visible light reflectance spectroscopy data from the LIMS Online Report Portal. Following Gong et al. (2023), the relative absorption band depth at 660 nm ($RABD_{660}$) was calculated using the algorithm of Rein and Sirocko (2002) (Text S4 in Supporting Information S1), reflecting the chlorins concentration and productivity. Measurements for uranium (U, ppm) and potassium (K, wt%) were deconvolved from Natural Gamma Radiation (NGR) data generated on IODP Expedition 363 (De Vleeschouwer, 2017; Rosenthal et al., 2018). Correlation matrix analyses and T-test were made by excel data analysis among different proxies. Spectral and cross-spectral analyses were performed using Analyseries (Paillard et al., 1996). Wavelet coherence analysis was performed using biwavelet package in R.

4. Results

The data set generated in this study reveals two main features: (a) a long-term climate transition over the last 2,000 kyr (Section 4.1) and (b) orbitally-paced variations during the 40 kyr world, from ~2,000 to ~ 1,300 ka (Section 4.2). In summary, a marked transition occurred in the productivity and terrigenous input fluxes from ~1,700 to ~1,400 ka (Figure S6 in Supporting Information S1), with both productivity and terrigenous input records shifting to lower values after the transition (Figures 2b and 2f). At orbital timescale, our results suggest that the variability of the productivity records occurs with a different dominant periodicity from that of terrigenous input during the 40 kyr world.

4.1. Long-Term Transition From ~1,700 to ~1,400 Ka

4.1.1. Terrigenous Input Records

At Site U1483, terrigenous input is mainly from the riverine run-off from the northwest Australian region (e.g., the Fitzroy and Ord Rivers) (Pei et al., 2021; Zhang et al., 2020), rather than from the South Indonesian archipelago, and includes minor aeolian dust components (Gingele & De Deckker, 2004; Kuhnt et al., 2015; Stuut et al., 2014). In this study, K wt% (MAR) and Log ((Al + K + Ti + Fe)/Ca) are used as indicators of the

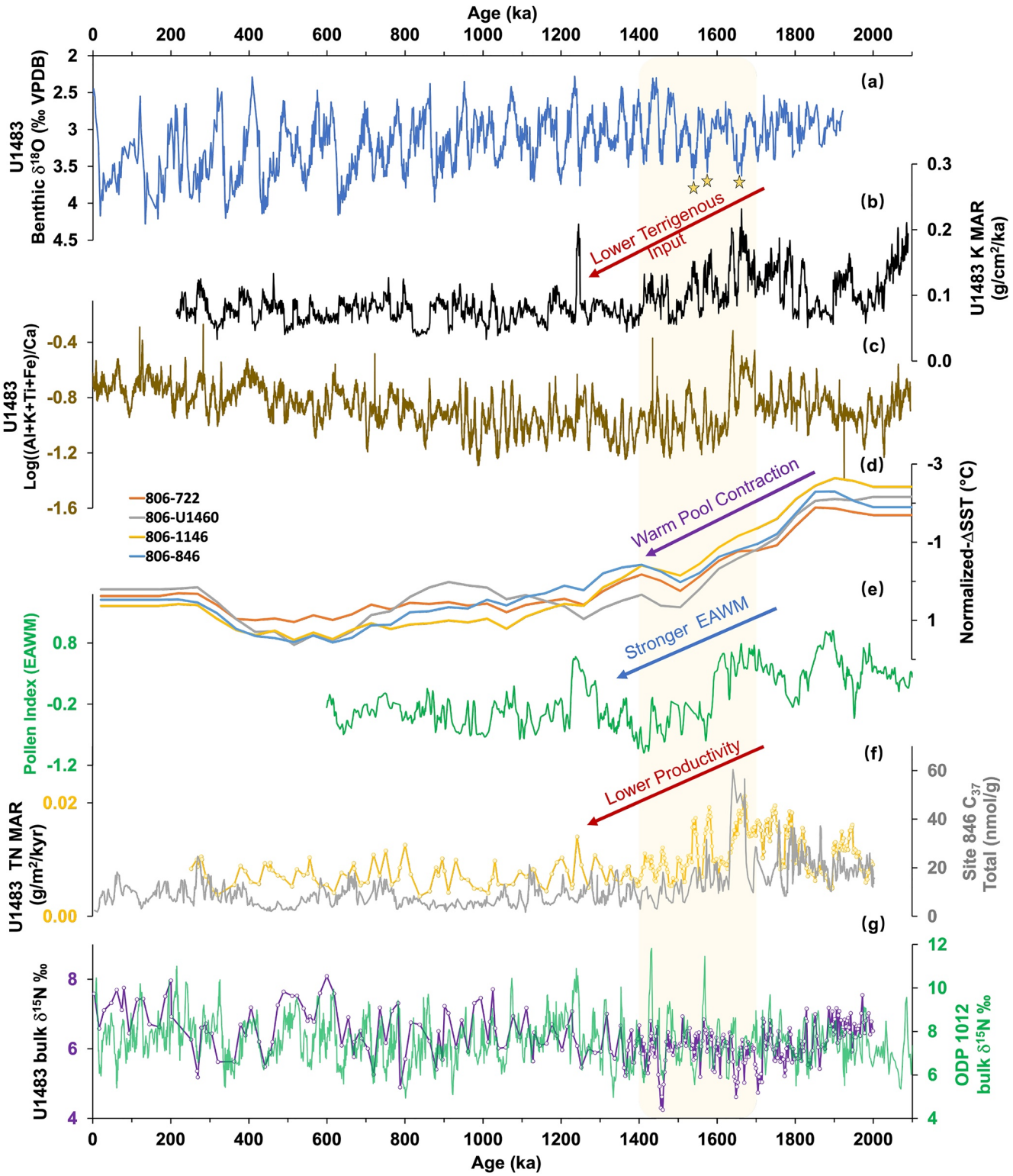

Figure 2. Long - term records generated at Site U1483 from this study are plotted with other related records over the last 2,000 kyr. (a) Benthic foraminiferal $\delta^{18}O$ from U1483 indicates global ice volume change and yellow stars indicate enhanced glaciations from 1,700 to 1,500 ka. Terrigenous input records from U1483 are inferred by K MAR (b) and Log ((Al + K + Ti + Fe)/Ca) (c). (d) Normalized ΔSST gradient in the IPWP is calculated by subtracting the SST records of Sites 722, U1460, 1,146, 846 from central IPWP Site 806. See original SST records and site map in Figure S15 in Supporting Information S1. (e) East Asian winter monsoon record is inferred by pollen index, data from Xin et al. (2020). (f) The productivity record (inferred by TN MAR) from U1483 is plotted with the productivity record based on C_{37} total (ng g sed^{-1}) from east equatorial Pacific Site 846, data from Lawrence et al. (2006). (g) Bulk $\delta^{15}N$ from U1483 is plotted with that from California margin Site 1,012, data from Liu et al. (2008). The yellow bar indicates the transition period from 1,700 to 1,400 ka.

terrigenous input at Site U1483. K wt% has been used previously as a proxy for riverine runoff and continental moisture in northwest Australian regions because clays and feldspars contain K-bearing aluminosilicates (Christensen et al., 2017; Ehrenberg & Svånå, 2001). Following Gong et al. (2023), the sum of elements aluminum (Al), potassium (K), iron (Fe) and titanium (Ti) (as proxies for the terrigenous derived sediment) normalized against calcium (Ca) (derived from marine biogenic carbonate), Log ((Al + K + Ti + Fe)/Ca), is also used as a proxy of terrigenous input in this study.

Over the last 2,000 kyr, a long-term transition is evident between ~1,700 and ~1,400 ka in terrigenous input flux (inferred by K MAR, Figure 2b) while Log ((Al + K + Ti + Fe)/Ca) exhibits an abrupt transition at ~1,600 ka (Figure 2c), after which the terrigenous input shifts to generally lower values. From ~2,000 to ~1,300 ka, the Log ((Al + K + Ti + Fe)/Ca) values are significantly positively correlated with K wt% (Figures 3g and 3h, $R^2 = 0.76$, $p < 0.001$), indicating that K wt% is not a result of dilution effects. $CaCO_3$ $wt\%_{EA}$ values are significantly negatively correlated with K wt% from ~2,000 to ~1,300 ka (Figures 3g and 3i, $R^2 = 0.66$, $p < 0.001$). According to the shipboard core description almost all the $CaCO_3$ in the sediment relates to marine primary productivity (without terrigenous or authigenic source) at Site U1483 (Rosenthal et al., 2018). At a water depth of 1,733 m, Site U1483 was above the lysocline during the mid-early Pleistocene; furthermore, the preservation of foraminifers at this site is excellent based on the shipboard report (Rosenthal et al., 2018), and thus, the effects of dissolution are minimal. At Site U1483, the high coherence among Log ((Al + K + Ti + Fe)/Ca), K wt% and $CaCO_3$ $wt\%_{EA}$ (Figures 3g–3i, Table 2) indicates that changes in the $CaCO_3$ $wt\%_{EA}$ is a result of varying amounts of dilution, low amounts of $CaCO_3$ implying high dilution of the sediment from terrigenous flux. Thus, K wt%, $CaCO_3$ $wt\%_{EA}$ and Log ((Al + K + Ti + Fe)/Ca) are used as indicators for terrigenous input. A striking shift occurred at ~1,640–1,625 ka in all three proxy records (Figures 3g, 3i), when $CaCO_3$ $wt\%_{EA}$ increased from 35% to 70%, K wt% decreased from 1.7% to 0.9% and Log ((Al + K + Ti + Fe)/Ca) decreased from −0.32 to −1.08, indicating a rapid decrease in terrigenous input within ~15 kyrs, corresponding to relatively warmer sea surface temperature and decreased global ice volume during the deglacial time. T-test reveals that all terrigenous input proxies exhibit significant changes ($p < 0.0001$) in their averages before and after 1,625 ka, indicating lower terrigenous input between 1,625 and 1,300 ka (Table 1).

4.1.2. Productivity Records

We use TN wt% (MAR) and $RABD_{660}$ as productivity proxies and use U and Log (Mn/S) as indicators for bottom water oxygen variations. The flux of TN (TN MAR) is calculated from the TN wt% and it reflects the primary production in the surface water. $RABD_{660}$ is derived from the visible light reflectance spectroscopy reflecting the chlorins concentration, which is reported to be highly correlated to marine organic carbon content and marine primary productivity (Harris et al., 1996; Rein & Sirocko, 2002), and can be used as a productivity indicator. Following Gong et al. (2023), we use the logarithmic ratios of the redox-sensitive elements manganese (Mn) and sulfur (S) (Log (Mn/S)) as proxies for bottom water oxygenation, with higher Log (Mn/S) corresponding to oxygenated environments. The concentration of authigenic U could reflect bottom-water redox conditions because U precipitates in anoxic environments due to its insolubility (Klinkhammer & Palmer, 1991). As nutrients are supplied to the surface by upwelling and organic matter is exported to the sea floor, the consumption of dissolved oxygen in the upper ocean increases, leading to anoxic environments and U precipitation in bottom waters. Thus, the concentration of U in the sediment is expected to be positively correlated to productivity. Since $CaCO_3$ in sediment at Site U1483 is marine-derived, the flux of $CaCO_3$ ($CaCO_3$ MAR) reflects the bio-carbonate productivity in this region.

Over the last 2,000 kyr, productivity (inferred by TN MAR) shifted to lower values from ~1,700 to ~1,400 ka (Figure 2f). We note that $CaCO_3$ MAR exhibits a different behavior to TN MAR, which increased first during 1,650–1,600 ka, while TN MAR started to decrease. Between 2,000 and 1,300 ka, TN wt%, $RABD_{660}$, Log (Mn/S) and U are significantly strongly correlated with each other (Figures 3b, 3d and 3e, Table 2, $p < 0.001$). The striking shift at ~1,650–1,625 ka, which appeared in the productivity records (inferred by TN wt% and $RABD_{660}$), is not pronounced in the bottom water oxygen records (inferred by U and log (Mn/S)), during which productivity decreased rapidly within ~25 kyrs (Figures 3b and 3c). T-test reveals that productivity and oxygen proxies show significant changes ($p < 0.0001$) in their averages before and after 1,625 ka, indicating a shift to lower productivity and higher bottom water oxygen from 1,625 to 1,300 ka (Table 1). Oxygen (2,000–1,300 ka) and productivity (typically after 1,650 ka) records show rhythmic variations during glacial-interglacial cycles, with higher TN MAR/U/$RABD_{660}$ and lower Log (Mn/S) values during glacial intervals, indicating high productivity during colder times (Figures 3b–3e).

10.1029/2023PA004683

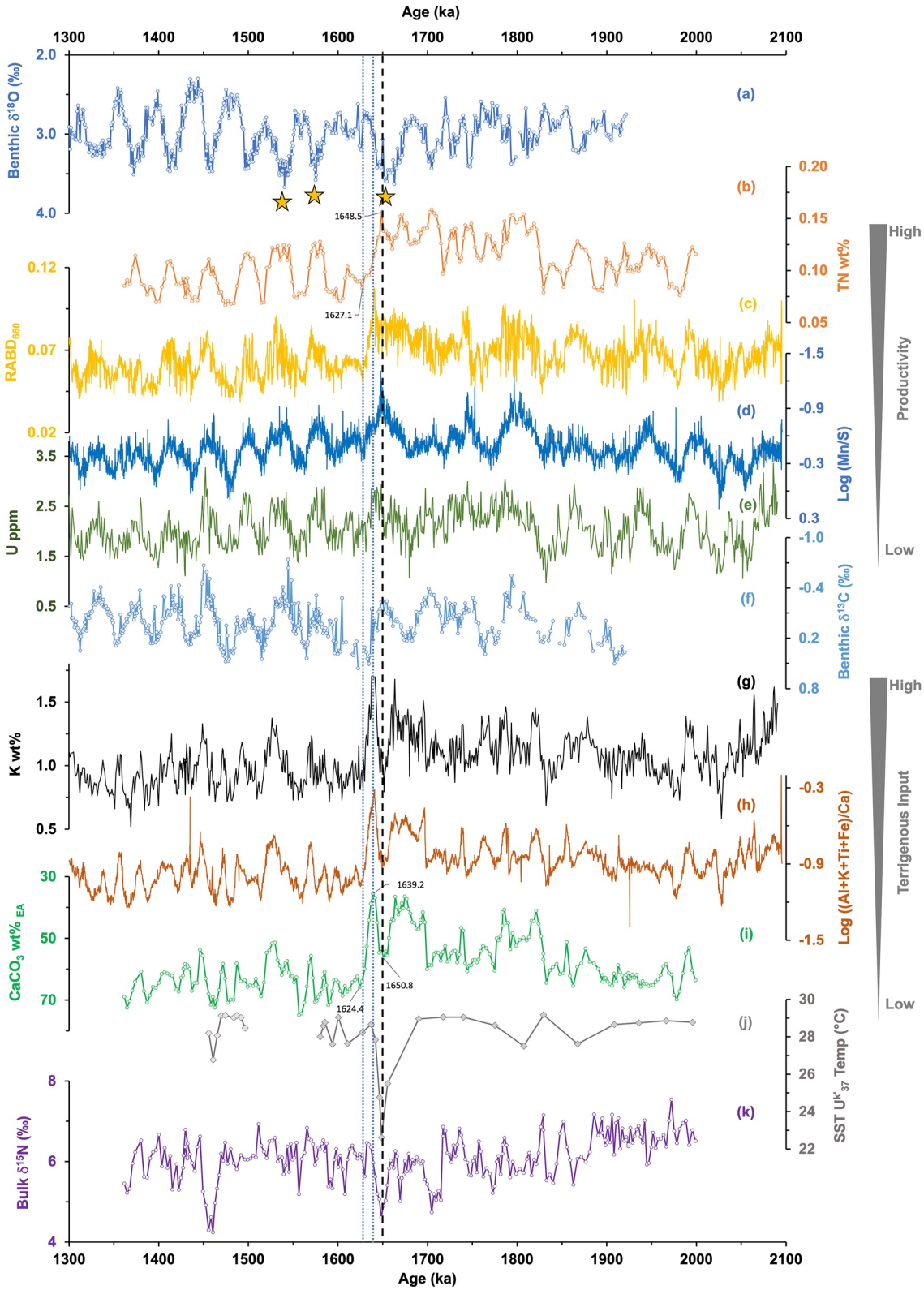

Figure 3.

Table 1
A T-Test Table Was Created to Analyze the Significance of a Change Between Averages for Each Proxy Before and After the Transition at 1,625 Ka From ~2,000 to ~1,300 Ka

T-test before and after the transition (1,300–2,000 ka)						
1,300–1,625 ka	1,625–2,000 ka	Average		*N* (# observations)		*P* (two-tail)	Average from old to young
LR04 $\delta^{18}O$		3.82	3.76	151	150	0.0500	increase
Benthic $\delta^{18}O$		3.00	3.02	338	180	0.5700	decrease
TN wt%		0.09	0.12	101	150	<0.0001	decrease
TN MAR		0.010	0.013	101	150	<0.0001	decrease
U ppm		1.99	2.10	377	557	0.0006	decrease
Log (Mn/S)		−0.43	−0.55	1,765	2,087	<0.0001	increase
$RABD_{660}$		0.06	0.07	1,323	1,566	<0.0001	decrease
K wt%		0.94	1.13	377	557	<0.0001	decrease
K MAR		0.10	0.13	377	557	<0.0001	decrease
$CaCO_3$ $wt\%_{EA}$		0.64	0.55	101	150	<0.0001	increase
MAR $CaCO_3$		6.70	5.83	101	150	<0.0001	increase
Log ((Al + K + Ti + Fe)/Ca)		−1.01	−0.82	1,764	2,087	<0.0001	decrease
Bulk $\delta^{15}N$		6.00	6.15	101	150	0.0240	decrease
Benthic $\delta^{13}C$		0.004	0.025	330	154	0.3333	decrease

Note. Except benthic $\delta^{18}O$, $\delta^{13}C$, U and bulk $\delta^{15}N$, all other proxies have significant changes ($p < 0.0001$) in their averages. All other productivity proxies (TN wt%, TN MAR, Log (Mn/S), $RABD_{660}$) and terrigenous input proxies (K wt%, K MAR, Log ((Al + K + Ti + Fe)/Ca), $CaCO_3$ $wt\%_{EA}$) indicate lower productivity and lower terrigenous input after the transition.

4.1.3. SST and Biomarkers

$U^{K'}_{37}$ values of the 32 selected samples analyzed range from 0.77 to 0.99 and TEX_{86} values range from 0.65 to 0.73. We obtained estimates of 22.6°C to 29.2°C based on $U^{K'}_{37}$ index using the Prahl and Wakeham (1987) calibration (Figure 3j) and of 26.5°C to 29.9°C based on TEX_{86} index using the Schouten et al. (2002) calibration (Figure S7 in Supporting Information S1). The $U^{K'}_{37}$ record generally agrees with the TEX_{86} record but larger SST decreases occur in the $U^{K'}_{37}$ record (~29°C to 22°C) compared to the TEX_{86} record (~28°C to 25°C) during the 1,650 ka shift (Figure S7 in Supporting Information S1). The intense surface cooling event occurring at ~1,650 ka is striking and robust (3 data points with $U^{K'}_{37}$ values <0.9) and the younger part of the $U^{K'}_{37}$-based SST record (from 1,500 to 1,450 ka) aligns with the corresponding glacial-interglacial cycle. C_{37} total (ng g sed^{-1}) is consistent with TN wt% (and other productivity records) and captures glacial-interglacial variability (Figure S7 in Supporting Information S1). Relatively low SST corresponds to relatively high productivity. The BIT index shows a decreasing trend from 2000 to ~1,450 ka, with a range between 0.09 and 0.18 and an average value of 0.14 (BIT < 0.2; Figure S7 in Supporting Information S1). The 1,650 ka shift in the BIT values corresponds to a minimum value of 0.09. Over the last 2,000 ka, there is no pronounced secular trend or long-term transition observed in our low-resolution SST records (Figure 3j); the intense cooling event occurring at 1,650 ka likely corresponds to the 1,650 ka shift in the productivity record and to relatively low values in the terrigenous input records (Figure 3 and Figure S7 in Supporting Information S1).

4.1.4. Bulk Nitrogen Isotopes

To distinguish between terrigenous and marine derived organic matter at Site U1483, we measured $\delta^{13}C_{org}$ and calculated TOC:TN ratios over the last 2,000 ka. Both TOC:TN (average = 11.03) and $\delta^{13}C_{org}$ values (average = −20.16‰) are within the typical range of marine organic matter (Meyers, 1994). $\delta^{13}C_{org}$ ranges

Figure 3. Orbitally-resolved records generated at Site U1483 over the interval ~2,000 to 1,300 ka. Benthic foraminiferal $\delta^{18}O$ (a) is plotted for chronological reference and yellow stars indicate enhanced glaciations from 1,700 to 1,500 ka. Productivity changes expressed as TN wt% (b) and $RABD_{660}$ (c); bottom water oxygen expressed as Log (Mn/S) (d) and U ppm (e). Benthic foraminiferal $\delta^{13}C$ (f) U. Terrigenous input changes are expressed as K wt% (g), Log((Al + K + Ti + Fe)/Ca) (h) and $CaCO_3$ $wt\%_{EA}$ (i). Low resolution SST (j) based on $U^{K'}_{37}$ index using the Prahl and Wakeham (1987) calibration and bulk $\delta^{15}N$ (k). Orbitally-resolved records show significant correlation with each other (Table 2); filtered records are shown in Figures S16 and S17 in Supporting Information S1. The black dash line indicates the unusual rapid event at ~1,650 ka, corresponding to the intense surface cooling event. Two blue dash lines indicate the rapid decline in terrigenous records from ~1,640 to 1,624 ka; numbers in panels b and i denote the key timing points of these rapid events.

Paleoceanography and Paleoclimatology

10.1029/2023PA004683

Table 2
Correlation Matrix Tables Were Created in Excel by Running a Regression Between Pairs of Proxies Before (Upper Table) and After (Bottom Table) 1,625 Ka (Using Corresponding Values due to Proxies With Different Resolution)

Correlation matrix before the transition 1,300–1,625 ka (R^2)	$CaCO_3$ wt% $_{EA}$	TN wt%	Bulk $\delta^{15}N$ (‰)	Corresponding K wt%	Corresponding U ppm	Corresponding log (Mn/S)	Corresponding Log((Al + K + Ti + Fe)/Ca)	Corresponding $RABD_{660}$
$CaCO_3$ wt%$_{EA}$	1.00							
TN wt%	0.06	1.00						
Bulk $\delta^{15}N$ (‰)	0.17	**0.00**	1.00					
corresponding K wt%	**0.53**	0.16	0.04	1.00				
corresponding U ppm	0.02	**0.36**	0.03	0.21	1.00			
corresponding Log (Mn/S)	0.02	**0.53**	0.00	0.08	**0.28**	1.00		
corresponding Log ((Al + K + Ti + Fe)/Ca)	**0.86**	0.11	0.16	**0.66**	0.05	0.05	1.00	
corresponding $RABD_{660}$	0.09	**0.27**	0.01	0.18	**0.15**	**0.28**	0.17	1.00

Correlation matrix after the transition 1,625–2,000 ka (R^2)	$CaCO_3$ wt% $_{EA}$	TN wt%	Bulk $\delta^{15}N$ (‰)	Corresponding K wt%	Corresponding U ppm	Corresponding log (Mn/S)	Corresponding Log((Al + K + Ti + Fe)/Ca)	Corresponding $RABD_{660}$
$CaCO_3$ wt%$_{EA}$	1.00							
TN wt%	**0.24**	1.00						
Bulk $\delta^{15}N$ (‰)	0.10	**0.47**	1.00					
corresponding K wt%	**0.57**	0.13	0.05	1.00				
corresponding U ppm	0.07	**0.26**	0.12	0.17	1.00			
corresponding Log (Mn/S)	0.09	**0.40**	**0.23**	0.07	**0.28**	1.00		
corresponding Log ((Al + K + Ti + Fe)/Ca)	**0.83**	0.16	0.07	**0.69**	0.07	0.05	1.00	
corresponding $RABD_{660}$	**0.29**	**0.26**	0.08	**0.27**	**0.22**	**0.20**	**0.27**	1.00

Note. The R^2 values are listed and negatively correlated is denoted by purple, positively correlated is denoted by black; significantly correlated ($p < 0.0001$) is highlighted in yellow, not significantly correlated is highlighted in blue. The values we care about are denoted by bold.

between −18.67‰ and −20.54‰ with no systemic variation and shows relatively constant values fluctuated around −20‰ (Figure S8 in Supporting Information S1). No correlation is shown between $\delta^{13}C_{org}$ and TOC/TN ($R^2 = 0.01$, $p < 0.001$) and between bulk $\delta^{15}N$ and $\delta^{13}C_{org}$ ($R^2 = 0.09$, $P = 0.7$) (Figure S8 in Supporting Information S1). These results suggest that the organic matter at Site U1483 is primarily of marine origin with minimal or little terrestrial influence, which is supported by the low BIT index (<0.2) (Figure S7 in Supporting Information S1), which is consistent with Holbourn et al. (2005) and Zhang et al. (2020). A significant positive linear correlation between TN wt% and TOC wt% ($R^2 = 0.74$, $p < 0.001$) with a y-intercept of 0.04 suggests minimal contribution from inorganic N (Figure S8 in Supporting Information S1). No correlation ($R^2 = 0.09$, $p < 0.001$) between bulk $\delta^{15}N$ versus TN wt% indicates minor alteration from early diagenesis on original $\delta^{15}N$ values (Figure S9 in Supporting Information S1).

Over the last 2,000 kyr, bulk $\delta^{15}N$ at Site U1483 ranges between 4.2 and 8.1‰ (average = 6.2‰) and exhibits no pronounced secular trend (Figure 2g). From 2,000 to 1,300 ka, there is no significant change in the average value of $\delta^{15}N$ before and after 1,625 ka (Figure 3k, Table 1). From 2,000 to 1,625 ka, bulk $\delta^{15}N$ is negatively correlated to TN wt% ($R^2 = 0.47$, $P < 0.001$) and U ($R^2 = 0.12$, $P < 0.001$), and positively correlated to Log (Mn/S) ($R^2 = 0.23$, $P < 0.001$). From 1,625 to 1,300 ka, bulk $\delta^{15}N$ is not correlated to TN wt% ($R^2 = 0.00$, $P = 0.9$) and to oxygen proxies. Bulk $\delta^{15}N$ shows little correlation to any other proxies (Table 2).

4.1.5. Benthic Foraminiferal Carbon Isotopes

Benthic foraminiferal $\delta^{13}C$ at Site U1483 ranges between −0.74‰ and 0.51‰ from 2,000 to 1,300 ka and there is no significant change in average value before and after ~1,625 ka (Figure 3f and Table 1), as for the bulk $\delta^{15}N$ records. Benthic $\delta^{13}C$ does not exhibit a pronounced long-term secular trend but shows a strong negative correlation with U values (Figure S10 in Supporting Information S1). Benthic $\delta^{13}C$ shows rhythmic variations following glacial-interglacial cycles after ~1,650 ka, with high $\delta^{13}C$ values during interglacial periods and low $\delta^{13}C$ values during glacial periods.

4.2. Orbital Variability

4.2.1. Spectral Analysis

Due to the appearance of the striking shift at ~1,650–1,625 ka (Figure 3), the records are divided into two parts (before and after 1,625 ka), and spectral analysis was performed on each of the time intervals (Figure 4 and Figure S11 in Supporting Information S1). The transition of spectral characteristics between ~1,650 and ~1,600 ka can also be seen in wavelet analysis (Figure S12 in Supporting Information S1). Spectral analyses reveal that variance in the terrigenous input records (inferred by Log ((Al + K + Ti + Fe)/Ca) and K wt%) is dominated by the 19–23 kyr (precession) periodicities throughout the period 2000–1,300 ka and 41 kyr (obliquity) periodicity occurred only after 1,625 ka (Figure 4). Productivity (inferred by TN wt%), bottom water oxygen (inferred by Log (Mn/S) and U) and benthic $\delta^{13}C$ show similar spectral characteristics to that of benthic $\delta^{18}O$ (Figure 4 and Figue S12 in Supporting Information S1). They show variability concentrated in the precession band before 1,625 ka followed by pronounced obliquity variability after 1,625 ka. Bulk $\delta^{15}N$ variability is concentrated in the precession band throughout the period 2000–1,300 ka with dominant obliquity variability occurring only after 1,625 ka (Figures S11 and S12 in Supporting Information S1).

4.2.2. Cross-Spectral Analysis and Phase Relationships

Wavelet coherence analysis was performed (Figure 5) and phase relationships were summarized (Figure 6). Productivity (inferred by TN wt%), bottom water oxygen (inferred by Log (Mn/S) and U) and benthic $\delta^{13}C$ exhibit similar behaviors to that of benthic $\delta^{18}O$, showing high coherency (>0.8) with obliquity from ~1,600 to 1,300 ka and some coherency with precession between ~1,900 and 1,700 ka. Terrigenous input (inferred by (Log ((Al + K + Ti + Fe)/Ca) and K wt%)) shows high coherency (>0.8) with precession from ~1,550 to 1,300 ka. Bulk $\delta^{15}N$ exhibits intermittent high coherency with precession through 2,000–1,300 ka and with obliquity only between ~1,500 and 1,350 ka. Besides being strongly coherent to benthic $\delta^{18}O$, benthic $\delta^{13}C$ exhibits high coherence (>0.8) with U ppm at the obliquity band from 2,000 to 1,300 ka and are out of phase with each other (with relatively high $\delta^{13}C$ values corresponding to relatively low U values).

10.1029/2023PA004683

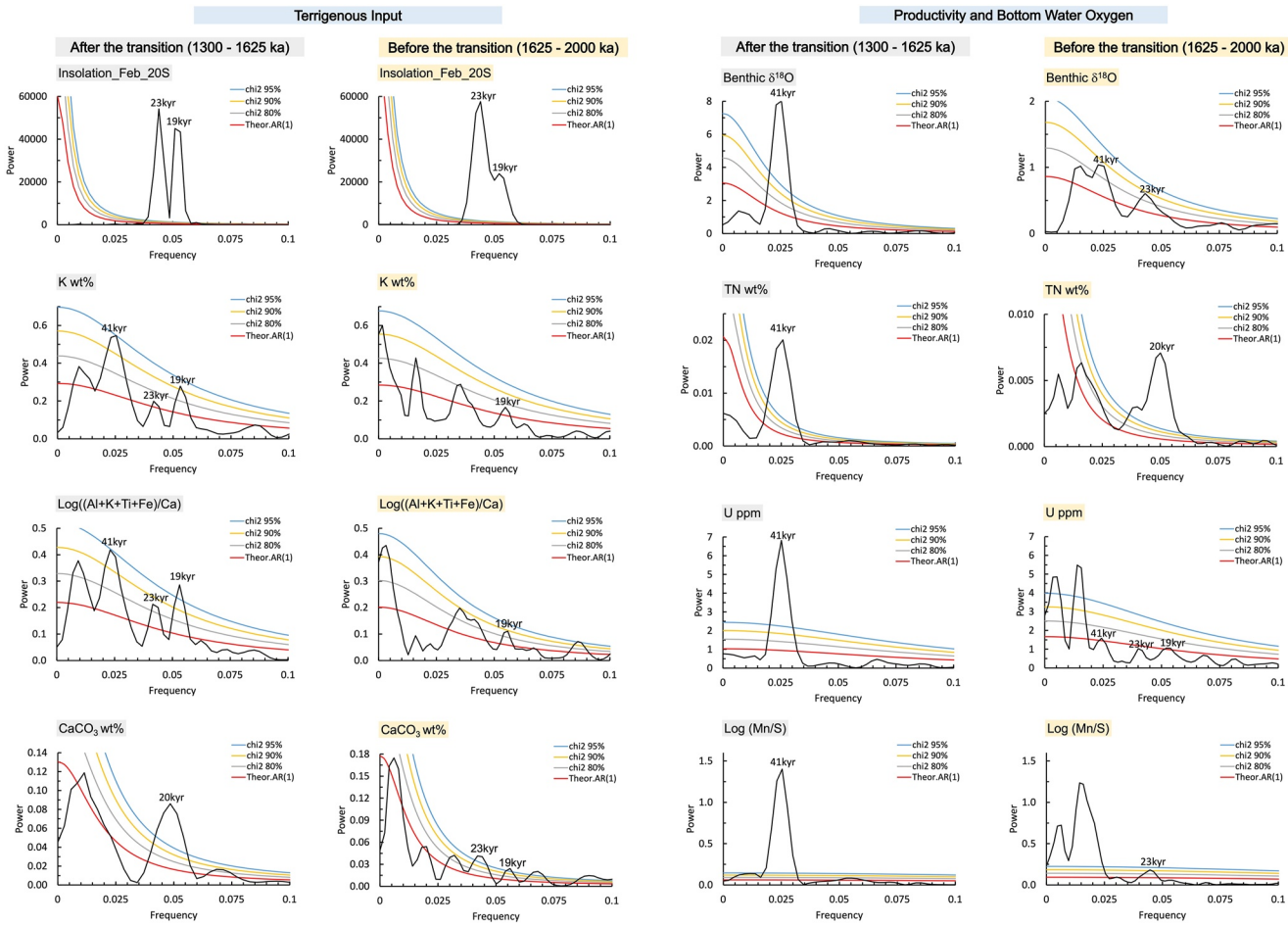

Figure 4. Spectral analysis results of different proxies before (highlighted by yellow) and after (highlighted by gray) ~1,625 ka. Except for insolation (Feb_20S), all other proxies are reconstructed from Site U1483. Spectral analysis was performed using REDFIT with Blackman-Harris window (Oversample = 2; Segments = 2) from software program Past 4 (Hammer, et al., 2001). Spectral analysis results of other proxies are shown in Figure S11 in Supporting Information S1.

5. Discussion

5.1. The 1,700–1,400 Ka Transition in Terrigenous Input

At Site U1483, terrigenous input flux (K MAR) exhibits long-term decline between ~1,700 and ~1,400 ka (Figure 2b) while Log ((Al + K + Ti + Fe)/Ca) exhibits an abrupt transition at ~1,600 ka (Figure 2c). Since long-term changes in Log ((Al + K + Ti + Fe)/Ca) might be affected by changes in marine carbonate production (Figure S5 in Supporting Information S1) (Gong et al., 2023), we think K MAR is a more robust proxy reflecting terrigenous input variations at Site U1483 and best defines the long-term transition in terrigenous input between ~1,700 and ~1,400 ka (Figure S6 in Supporting Information S1). As terrigenous input at Site U1483 is primarily from riverine sources of the northwest Australian region, the shift to lower terrigenous input from ~1,700 to ~1,400 ka could be a result of (assuming no change in the river catchment system): (a) a final step in the aridification of northwest Australia and consequently less riverine input to the ocean due to decreased precipitation; or (b) a transition to a wet climate and enhanced vegetation cover in this region resulting in less riverine sediment load. Most available Australian paleoclimate records monitor central and southeast Australian conditions (Christensen et al., 2017; Kershaw et al., 2017; Martin, 2006); few records are from coastal northwest Australia, and there are no published records extending to the mid-early Pleistocene (40 kyr world), the time period of this study. In northwest Australia, a transition to an arid landscape was inferred by the replacement of the casuarinaceous forests with grasslands by the late Pleistocene (Martin & McMinn, 1994), but these studies do not cover the 1,700–1,400 ka interval. Although there are no continental paleoclimate studies from northwest Australia that span the same

10.1029/2023PA004683

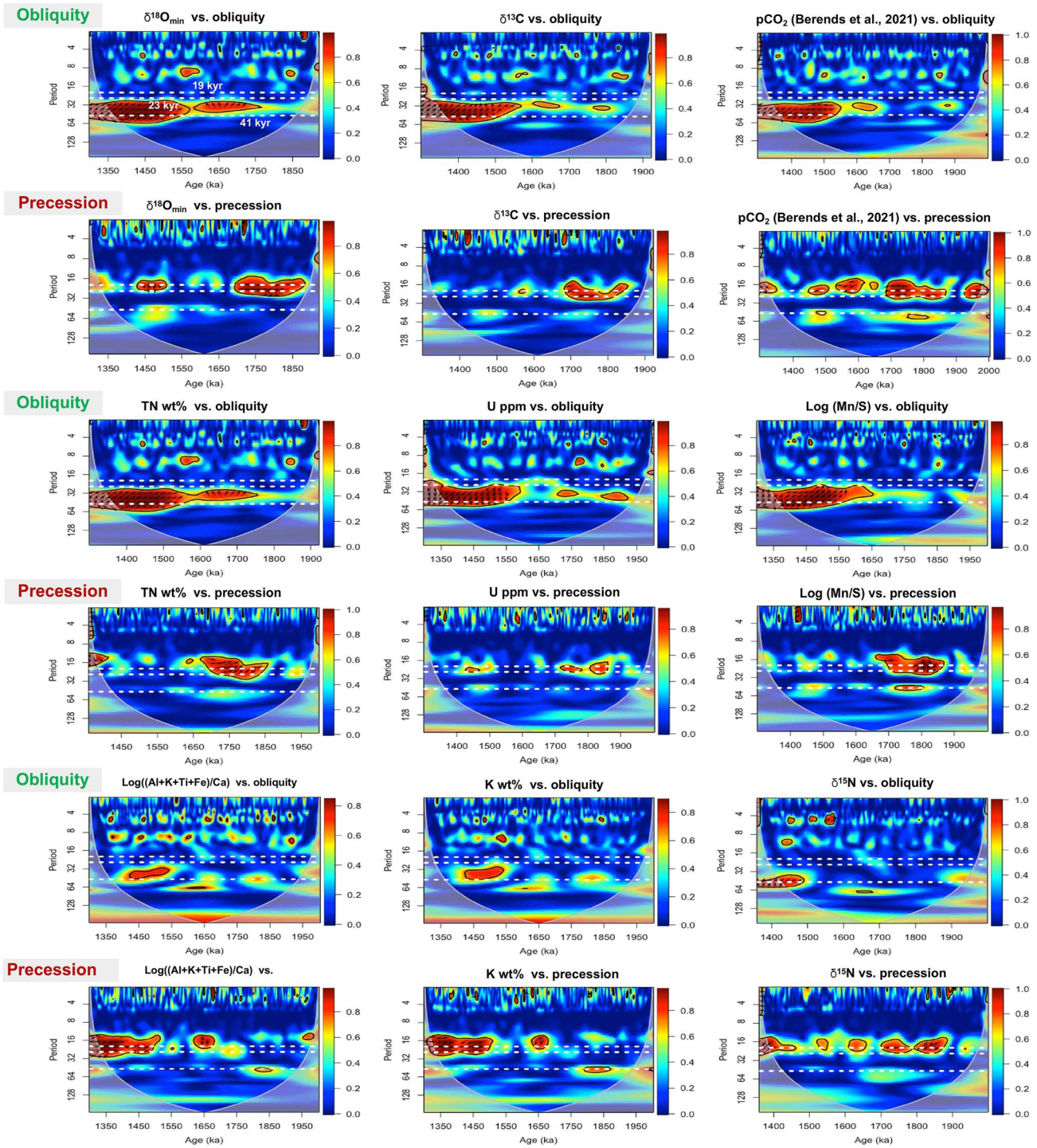

Figure 5. Wavelet coherence analysis between proxies at Site U1483 (except the pCO_2 records from Berends et al. (2021)) and orbital forcing (obliquity and precession) from ~2,000 to 1,300 ka. Wavelet coherence analysis was performed using biwavelet (wtc) package in R. The white dash lines indicate 19, 23 and 41 kyr.

time interval as our study, evidence from other regions of Australia strongly suggests increasing aridity during the Pleistocene (Christensen et al., 2017 and references therein; Kershaw, Moss, & Van Der Kaars, 2003). First, an overall decreasing trend of precipitation in Australia through the Pleistocene has been proposed (Martin, 2006). Second, an enhanced aridification at ~1,500 ka at Lake Bungunniain in southern Australia (McLaren et al., 2012) and a transition to aridity possibly at 1,600 ka at Lake Amadeus in the central Australia have been reported (Chen

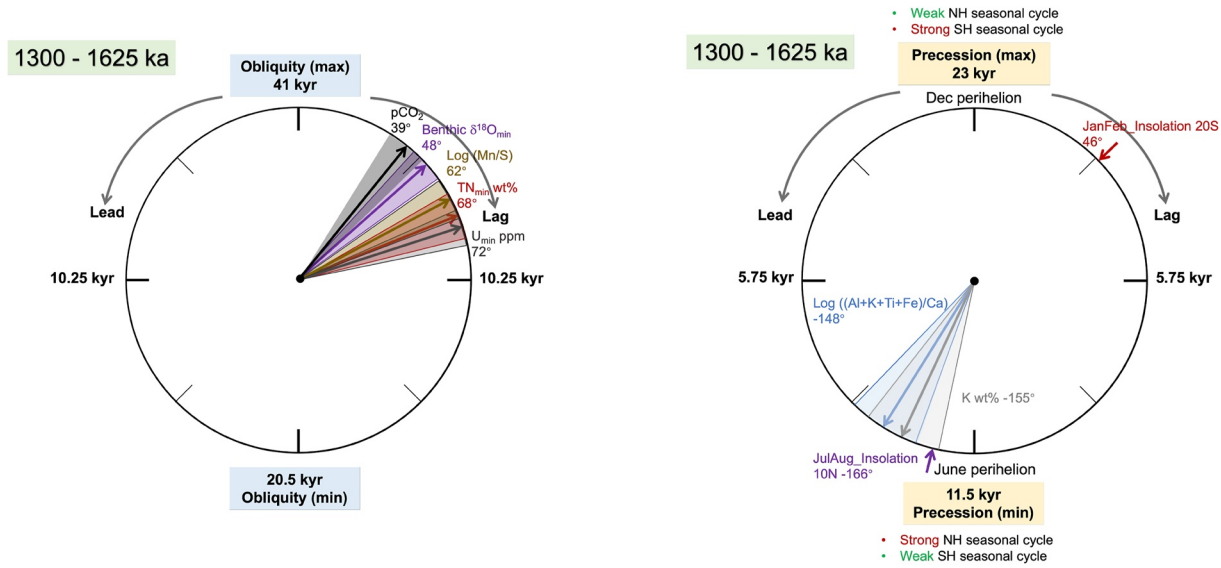

Figure 6. Phase wheel results of cross-spectral coherence and phase relationships at the obliquity band (left) and precession band (right) from 1,300 to 1,625 ka. Phase relationships are calculated by conducting cross-spectral coherence analysis between U1483 records (and insolation) and orbital templates (obliquity and precession) and are only shown when coherence >0.8. Clockwise phases indicate lags and counterclockwise phases indicate leads. Shaded areas delineate error margins for U1483 records and modeled atmospheric pCO_2 from Berends et al. (2021). We acknowledge that there are established phase lags built in the LR04 age model and the tuned benthic $\delta^{18}O$ record displays almost the same spectral characteristics as the LR04 stack. In this study, we assume the built phase lags in the age model are good assumptions and the relative phase relationships between proxy records from the same site are robust.

& Barton, 1991). Therefore, all the evidence points to increasing aridity and reduced runoff, rather than a shift to a wetter continental northwest Australia, as the most likely explanation for a decrease in terrigenous input from 1,700 to 1,400 ka in our records (Figures 2b and 2c). This is consistent with the interpretative framework used by Christensen et al. (2017) that K wt% can be used as a continental moisture proxy, with low K wt% corresponding to drier conditions and vice versa. This is also consistent with other previous paleoceanographic studies, which indicate that increasing aridity off the northwest Australian coast from ∼1,700 to ∼1,400 ka corresponds to reduced ITF inferred from cooling SSTs (He et al., 2021; Petrick et al., 2019; Smith et al., 2020).

The rainfall pattern in northwest Australia could be influenced by three main processes. (a) The dynamics of the Australian summer monsoon may play a major role since about three quarters of the rainfall in northern Australia is registered during the monsoon season in western Australia at present (Chang et al., 2006; Suppiah, 1992). (b) The strength of the ITF, which brings heat and moisture from the equatorial Pacific, can influence the land-sea temperature gradient and precipitation patterns in northwest Australia (Christensen et al., 2017; Ishiwa et al., 2019). Model results and long-term geological records have shown that the restriction of the ITF would lead to a significant reduction of rainfall in Australia and contribute to its aridity (Christensen et al., 2017; Stuut et al., 2019). (c) The large-scale tropical hydroclimate, including the thermal evolution of the IPWP and Walker circulation dynamics, can impact the Australian climate. Walker circulation is known to play a predominant role in hydroclimate changes in the equatorial Indo-Pacific region (through modifying ENSO events) and is closely linked to SST pattern across the Pacific (Dang et al., 2020; Kaboth-Bahr & Mudelsee, 2022). In summary, the shift to lower terrigenous input during 1700–1400 ka, indicating a major step of aridification in the northwest Australian region, could be a result of (a) a reduction in the strength of the Australian summer monsoon; (b) a reduction of the intensity of the ITF; (c) a shift in the thermal evolution of the warm pool and Walker circulation. These three possibilities are discussed below, although it is worth pointing out that the monsoon systems, the ITF, and Walker circulation interact with each other, and these mechanisms are not necessarily mutually exclusive.

5.1.1. Shift in the Asian-Australian Monsoon System

The first possible candidate causing the 1,700–1,400 ka transition in the precipitation in northwest Australia is a shift in the monsoon system. The East Asian winter monsoon (EAWM) is related to the Siberian high and is primarily driven by the high latitude forcing in the North Hemisphere (NH); the strong cold winds could flow across the equator and influence the summer monsoon and hydroclimate in the South Hemisphere (SH) (Liu

et al., 2015). In this context, we expect that the Australian summer monsoon correlates to the EAWM which can be tracked by Asian winter monsoon records (An, 2000). An intensification of the EAWM at ~1,600 ka has been widely documented in loess and pollen records (Ding et al., 2002; Sun et al., 2006, 2019; Xin et al., 2020) and has been associated with a global climate cooling trend (Xin et al., 2020). The timing of the intensification in the EAWM (inferred by the pollen index) (Figure 2e) roughly occurs during the transition to drier conditions in northwest Australia inferred from the terrigenous input record at Site U1483 (Figures 2b and 2c). This is the opposite of what we would expect if the observed decrease in terrigenous input was primarily driven by the coupling of the Australian summer monsoon to changes in the strength of the EAWM. Therefore, we conclude that the shift in the monsoon systems did not directly drive the long-term transition observed in our terrigenous input records but could contribute to it in a complicated way through the interactions with the ITF (see Section 5.1.3 below).

5.1.2. Shift in the Strength of the ITF

The second possible explanation for changes in precipitation in northwest Australia from ~1,700 to ~1,400 ka is the restriction of the ITF. The restriction of the ITF has been implicated in previous studies as the cause of intense cooling and aridification sometime between 1700 ka and 1,500 ka at northwest/west Australian sites (U1460, U1461, U1463) (Christensen et al., 2017; He et al., 2021; Petrick et al., 2019; Smith et al., 2020). Consistent with these other studies, our records at Site U1483 not only show a similar transition in terrigenous input (Figure S13 in Supporting Information S1) but also exhibit the intense surface cooling event (Figure S14 in Supporting Information S1) at ~1,650 ka contemporaneous with relatively low terrigenous input (Figures 3g–3j). Previous studies attributed the surface cooling events to a weakening of the ITF driven by global sea level changes and ongoing tectonic activities (Petrick et al., 2019) and proposed that increasing northwest Australian aridity was driven by the progressive constriction of the ITF during the Plio-Pleistocene, which resulted in lower SSTs and reduced moisture reaching this region (Christensen et al., 2017; Smith et al., 2020). Site U1483 is directly influenced by the ITF and, compared to other sites studied, better located to track changes in the ITF. The ITF transport is determined by the surface pressure gradient between the Pacific and Indian Ocean, which is influenced by changes in sea level, wind-forcing (e.g., the strength of the East Asian monsoon) and buoyancy forcing (Feng et al., 2018). Based on the records at Site U1483, we discuss two plausible mechanisms responsible for the restriction of the ITF from ~1,700 to ~1,500 ka; one mechanism is related to the effects of sea level change and the other to Asian monsoon-related circulation.

Sea level changes are thought to drive the flow in the Timor passage on glacial/deglacial timescales during the Holocene and Pleistocene (Kuhnt et al., 2004). From ~1,700 to ~1,500 ka, the benthic $\delta^{18}O$ record show enhanced glaciations (Figure 2a), indicating decreasing glacial sea levels, which would contribute to restriction of the ITF and reduce moisture supply and precipitation of the northwest Australian region. Specifically, the observed intense cooling event at ~1,650 ka occurs during the first enhanced glaciation (MIS 58) (Figures 3a and 3j), consistent with the strong coupling between the surface cooling and the reduction of the ITF proposed in previous studies (He et al., 2021; Petrick et al., 2019; Smith et al., 2020). In addition, sea level reconstructions based on measurements and simulations show decreasing glacial sea levels changing from −50 to −85 m from ~1,700 to ~1,500 ka (Berends et al., 2021 and references therein), supporting the idea that global sea level change contributed to the reduction of the ITF and the aridity of northwest Australia during this period.

Changes in the strength of the Asian monsoon system could also affect the intensity of the ITF; thus, it is important to consider how the ITF was impacted during the transition in the strength of the EAWM from ~1,700 to ~1,500 ka (see Section 5.1.1). In the modern ocean, the strength of the ITF varies seasonally responding to the wind forcing (Kuhnt et al., 2004) and the important negative feedback between the Asian monsoon and the intensity of the ITF has been proposed (Gordon et al., 2003). During the boreal winter (Australian summer), the northwesterly Asian winter monsoon drives buoyant, low-salinity Java Sea surface water into the southern Makassar Strait, creating a northward pressure gradient in the surface layer, which inhibits the overall strength of the ITF, cooling the east Indian Ocean and strengthening the Asian winter monsoon (Gordon et al., 2003). In this context, the intensification of the EAWM at ~1,600 ka, as an indication of intensified Asian winter monsoon during this time (An, 2000), may have weakened the ITF and contributed to increase aridity in northwest Australia. Moreover, the ongoing tectonic activity in the Indonesian archipelago through the Pleistocene could also potentially contribute to the weakening of the ITF during this time (Petrick et al., 2019 and references therein).

In summary, lower glacial sea levels, negative Asian monsoon-ITF feedbacks and potential tectonic changes through the Pleistocene could result in significant restriction of the ITF from ~1,700 to ~1,400 ka and contribute to the increased aridity of northwest Australia after the transition.

5.1.3. Shift in the Walker Circulation and Warm Pool Contraction

The third possible mechanism for changes in precipitation in northwest Australia from ~1,700 to ~1,400 ka is related to the Walker circulation and evolution of the IPWP, which are thought to be important drivers of the hydrological cycle in the Indo-Pacific region (e.g., Brierley et al., 2009; Hollstein et al., 2018). Several studies found that the modern pattern of east–west SST asymmetry in the tropical Pacific, was not established until at ~1,600–1,500 ka (Berner et al., 2022; Kaboth-Bahr & Mudelsee, 2022; Lawrence et al., 2006; Ravelo et al., 2006; Wara et al., 2005), indicating a steplike intensification in the Walker circulation during this time. It has been reported that the increasing zonal SST gradient across the equatorial Pacific is tightly linked to increasing meridional SST gradient via the wind-driven circulation and upper-ocean stratification (Fedorov et al., 2015), which affects precipitation changes, including reduced rainfall in northwest Australia (Brierley et al., 2009; Burls & Fedorov, 2017). The IPWP underwent a steplike transition between 1,800 and 1,600 ka (Bali et al., 2020; Martínez-Garcia et al., 2010) from an expanded tropical warm pool which persisted in the Pliocene to a reduced warm pool, due to the expansion of the subpolar water masses (Martínez-Garcia et al., 2010). To investigate the connection between the warm pool change and the transition observed at Site U1483, we evaluate changes in SST gradients between the IPWP center and its edge (Figure 2d and Figure S13 in Supporting Information S1). The SST record from the warm pool (Site 806) shows a gradual increase in SSTs compared to those from off-center sites (Sites 722, U1460, 146 and 846), which exhibit subtle decreases/increases between 1800 and 1,500 ka (Figure S15 in Supporting Information S1). Our results suggest that the enhanced zonal SST gradient (White & Ravelo, 2020) is coupled to enhanced gradients between the center of the warm pool and peripheral sites from ~1,800 to 1,500 ka (Figure 2d). This result indicates that the contraction of the warm pool starting at ~1,800 ka and culminating in the establishment of the modern warm pool pattern at ~1,500 ka, is closely coupled to the development of the modern cold tongue and Walker circulation (Kaboth-Bahr & Mudelsee, 2022; Martinez-Garcia et al., 2010).

The timing of the observed warm pool contraction (~1,800 to 1,500 ka) (Figure 2d) overlaps with the timing of the observed aridification (Figures 2b and 2c) of northwest Australia at 1,700–1,400 ka. Contraction of the warm pool enhanced both the zonal and meridional temperature contrast and strengthened the atmospheric meridional Hadley circulation causing stronger trade winds (Brierley et al., 2009). Model simulations have shown that the strength of the meridional SST gradients, particularly between the subtropics and the tropics, plays a key role in driving hydrological changes in the warm Pliocene experiment through controlling the strength of the Hadley circulation (Brierley et al., 2009; Burls & Fedorov, 2017). These simulations point out that the wetter subtropics in the Pliocene are the result of weakened equatorward moisture transport due to the reduced meridional circulation (Burls & Fedorov, 2017). Therefore, the intensification in the large-scale meridional SST gradient and the warm pool contraction from 1,800 to 1,500 ka, could have induced an enhanced wind-driven meridional moisture transport resulting in reduced precipitation in the subtropics such as the aridification in northwest Australia observed in our records. While intensification of the Walker circulation and enhanced trade winds between 1,500 and 1,800 ka could theoretically cause an increase in the ITF transport, existing SST records (e.g., He et al., 2021; Petrick et al., 2019; Smith et al., 2020) documenting a weakening of the ITF suggest that sea level change was a more important control on the ITF during this time.

The balance of evidence suggests that the contraction of the warm pool and associated changes in rainfall patterns combined with the restriction of the ITF due to sea level changes and the Asian monsoon feedback reduced moisture supply to northwest Australia, leading to aridification and reduced terrigenous flux at Site U1483 from ~1,700 to ~1,400 ka.

5.2. The 1,700–1,400 Ka Transition in Productivity

The long-term evolution of productivity, monitored using TN MAR (Figure 2f), indicates a decrease in productivity from ~1,700 to ~1,400 ka. Within this interval, there is a marked shift at ~1,650 ka in the other productivity indicators, total C_{37} (Figure S7 in Supporting Information S1) and $RABD_{660}$ (Figure 3c and Table 1), and a less distinct shift toward higher values in the indicators of bottom water oxygen conditions, Log (Mn/S) and U (Figures 3d and 3e and Table 1). The $\delta^{13}C_{org}$, bulk $\delta^{15}N$ and TOC:TN ratios suggest minimal terrigenous derived organic matter and inorganic N contribution at Site U1483 (see Section 4.1.4 and Figure S8 in Supporting Information S1); thus we

interpret the TN MAR record as reflecting a primarily marine source, consistent with palynological analysis from the nearby Site MD01-2378 (Holbourn et al., 2005). Generally, our productivity proxies show significant correlation with oxygen proxies from 2,000 to 1,300 ka (Table 2), probably explained by the fact that dissolved oxygen consumption is influenced by surface productivity with relatively low oxygen related to high productivity and vice versa. Differences between these proxy records might be related to independent changes in the deep circulation or preformed oxygen.

In the modern ocean, the upper ocean mixing and productivity in the Timor Sea are affected by the ITF transport and monsoonal winds. Thus, to explain the 1,700–1,400 ka transition observed in the productivity-related proxy records (Figures 2f, 3b–3e), we explore three processes. (a) The Australian winter offshore monsoon winds lead to intense Ekman transport and enhanced upwelling and productivity along the coast in northwest Australia (Beaufort et al., 2010; Susanto et al., 2001). The strong precession cycles in productivity changes driven by offshore monsoon winds have been documented in the Timor Sea and Banda Sea over the late Pleistocene by Holbourn et al. (2005) and Beaufort et al. (2010). (b) An enhanced ITF would increase the upper ocean stratification along the west Australian coast by bringing warm and fresh water from the Pacific and suppress the coastal upwelling and productivity. During cold and dry glaciations, lower sea levels resulted in a restricted and weakened ITF and led to an increase in upwelling and productivity (Susanto et al., 2001). It has been shown that productivity in the Timor Strait is strongly inversely proportional to the intensity of ITF over the last glacial cycle (Müller & Opdyke, 2000). (c) The nutrient supply from Pacific source water can affect productivity. The upper waters in the Timor Sea mainly originate from the North Pacific through the ITF and the intermediate water comprises Indonesian intermediate water and the AAIW from the South Pacific (Chen et al., 2022 and references therein). In summary, the transition to lower productivity from ∼1,700 to ∼1,400 ka at Site U1483 could be the result of (a) a reduction of the strength of the Australian winter monsoon; (b) an increase in the intensity of the ITF; and/or (c) the reduction of nutrient supply from the source water.

5.2.1. Shift in Australian Winter Monsoon and in the ITF

The intensification in Walker and Hadley circulation (see Section 5.1.3) and the reduction in the ITF (see Section 5.1.2) would be expected to be accompanied by an increase in productivity from ∼1,700 to ∼1,400 ka, which is the opposite of what is observed in our productivity related records (Figures 2f, 3b–3e). Enhanced Walker and Hadley circulation strengthen the trade winds, thus there was likely a strengthening in the Australian winter monsoon (Wang et al., 2005) at the transition. This is supported by observations of the intensification of coastal upwelling off the northwest Australian coast since ∼1,700 ka (Smith et al., 2020), however this intensification of upwelling is not coupled to an increase in productivity. The restriction of the ITF documented during ∼1,700–1,500 ka is expected to enhance the upwelling and the productivity through reducing the stratification of the upper ocean in the Timor Sea. However, while the reduction of the ITF could contribute to surface cooling and the decrease in the terrigenous input and precipitation (see Section 5.1.2), it cannot explain the reduction observed in our productivity records (Figures 2f, 3b–3e and Table 1). Therefore, the shift to lower productivity during the transition was not forced by physical processes such as those related to the winter monsoon and the effects of the ITF on stratification; rather, the lower productivity has to be related to reduced nutrient concentration of the source water.

5.2.2. Productivity Changes Related to Source Water Process

The development of modern-like Walker circulation and IPWP at roughly 1,700–1,400 ka was accompanied by transitions observed in many global oceanic and continental records (Berner et al., 2022; Etourneau et al., 2009, 2013; Fang et al., 2020; Lawrence et al., 2006; Li et al., 2011; Ravelo et al., 2004; Wang et al., 2010). Our U1483 productivity record shows striking similarities to that from ODP Site 846 located in the east equatorial pacific (EEP) (Figure 2f) (Lawrence et al., 2006). At Site 846, the $U^{K'}_{37}$- based SST record shows cooling at ∼1,650 ka (Figure S14 in Supporting Information S1) and the total C_{37} productivity record exhibits a transition between 1,700 and 1,400 ka, which is similar to our U1483 record and to records at Site ODP 1012 in the California Margin (Liu et al., 2008) and other EEP sites (Site 1239 and 1240) (Etourneau et al., 2013). Furthermore, the productivity records from EEP Site 846 and our northwest Australian Site U1483 both show similar glacial-interglacial patterns after ∼1,600 ka. These similarities among distant sites support the idea that the transition in the productivity records is primarily driven by similar nutrient source water changes instead of separate regional changes.

Lawrence et al. (2006) propose that the transition to lower productivity in the mid-Pleistocene might be related to the development of the modern Southern Ocean opal belt at ∼2,000 ka (Cortese et al., 2004), consistent with

the idea that the Southern Ocean may play an important role in the 1,600 ka Plio-Pleistocene transition (Wang et al., 2010). Etourneau et al. (2013) attributed the termination of the high productivity interval at EEP sites to enhanced regional denitrification and decreased nutrient leakage from the high latitude regions, associated with high productivity in the Southern Ocean due to iron fertilization between ~1,700 and 1,600 ka (Martínez-Garcia et al., 2011). As such, relatively low nutrient water was transported to the low latitude regions via the mode and intermediate waters and limited production in the equatorial Pacific (Lawrence et al., 2006; Martínez-Garcia et al., 2011). Since water at Site U1483 is mainly derived from the Pacific, including North Pacific upper waters and AAIW, we concur with the previous interpretations that the transition in the productivity records observed at Site U1483 could be attributed to the decreased nutrient supply in the water sourced from high latitude regions, related to the increased production in the Southern Ocean due to the enhanced iron fertilization (Martínez-Garcia et al., 2011) and extensive diatom mat development at ~1,900 ka (Cortese & Gersonde, 2008). We note that the pronounced decrease TN MAR occurred while $CaCO_3$ MAR increased at 1,600–1,650 ka at Site U1483 (Figure S5 in Supporting Information S1), likely indicating an ecosystem shift during this period. We conclude that the transition in productivity at Site U1483 from ~1,700 to ~1,400 ka reflects changes in Pacific source waters, associated with Southern Ocean biogeochemical dynamics and the nutrient redistribution of the global ocean.

5.3. Orbital Variability

Orbital resolution records generated between ~2,000 and ~1,300 ka at Site U1483 reveal a shift in orbital characteristics between ~1,650 and 1,625 ka. Due to the appearance of this striking shift spectral analysis was performed on two time intervals (before and after ~1,625 ka). This shift, explained in more detail in the following sections is characterized by (a) a change in terrigenous input and productivity orbital variability from weak cyclicity prior to 1,625 ka to strong cyclicity after 1,625 ka (Figure 4); (b) a change from weak coherence between terrigenous input proxies and precession prior to ~1,650 ka to stronger coherence after ~1,650 ka (Figure 5); (c) a change in productivity and oxygen variability from being coherent to orbital forcing at the precession band prior to ~1,650 ka to being coherent with orbital forcing at the obliquity band after ~1,650 ka (Figure 5). In all, the orbital variability analysis reveals a significant transition period during which the proxy records started to become more sensitive to orbital forcing between ~1,650 and 1,625 ka (see Section 5.3.5). In the sections below, we discuss the processes potentially responsible for the orbital scale variability at Site U1483.

5.3.1. Terrigenous Input Obliquity-Band Variability

Although terrigenous input records (inferred by K wt% and Log ((Al + K + Ti + Fe)/Ca)) at Site U1483 show obliquity-paced variation from 1,625 to ~1,300 ka (Figure 4, confidence >90%), they are weakly coherent (coherence <0.8) with obliquity during this period (Figure 5), similar to results over the last 410 kyr at the same site (Zhang et al., 2020). Gong et al. (2023) found that precipitation and terrigenous input variation (inferred by Log ((Al + K + Ti + Fe)/Ca)) at Site U1483 was dominated by precessional signal from 1,600 to ~950 ka, which partially overlaps with the interval of 1,625–1,300 ka that we focus on in this study. Our results indicate that the orbital variability of precipitation at Site U1483 evolved: from ~1,600 to 1,300 ka, it exhibits stronger obliquity cyclicity; from 1,300 to ~950 ka, it exhibits pronounced precession cyclicity. Therefore our results suggest that precipitation variations in northwest Australian are driven by combined precession and obliquity forcing. The weak coherency between our records and obliquity is likely related to a non-stationary phase relationship between terrigenous input and obliquity forcing (Figure S16 in Supporting Information S1). In contrast to the nearly anti-phase relationship between the rainfall record and obliquity forcing over the last 410 kyr at Site U1483 (Zhang et al., 2020), our terrigenous input records are roughly aligned with obliquity variations from 1,625 to ~1,300 ka (Figure S16 in Supporting Information S1), consistent with wetter interglacial periods (obliquity max) and drier glacial periods (obliquity min), which is supported by continental climate variability in Australia during the Pleistocene that have been attributed to high sea levels and potential enhanced monsoon activity (Kershaw, Moss, & Van Der Kaars, 2003, Kershaw, van der, et al., 2003; Martin, 2006 and references therein). The occurrence of increased terrigenous input roughly during the early part of interglacials (Figure S16 in Supporting Information S1), suggest that the distance between the adjacent river mouths and Site U1483 was not the main control on terrigenous input variation during this time. There is little obliquity forcing in the local low-latitude insolation (Figure 4), but obliquity is significant in NH high-latitude insolation driving glacial-interglacial sea level variability in the 40 kyr world. In this context, the obliquity signal in our terrigenous input records could be related to obliquity band variations

in (a) the Walker circulation and the ITF regulated by sea level effects on the exposure of the Maritime continent; (b) the Walker circulation and the ITF driven by tropical Pacific dynamics; (c) latitudinal migration of the ITCZ.

The first two mechanisms causing the obliquity-paced variability in the northwest Australian precipitation and terrigenous flux are related to changes in the Walker circulation and the ITF; these two processes produce opposite effects. In the first mechanism, precipitation in the warm pool region is driven by the Walker circulation regulated by the landmass configuration of the Maritime Continent on glacial-interglacial timescales (DiNezio et al., 2016; DiNezio & Tierney, 2013; Du et al., 2021). Based on the last glacial maximum (LGM) records and model simulations, low sea level in the glacial times led to more land exposure of the northwest Australian shelf and Sunda and Sahul shelves [shallow <50 m] (Figure 1a), inducing reduced convection due to enhanced land cooling over exposed areas, thus leading to weakening of the ascending branch of the Walker circulation over the Maritime continent and dry eastern Indian Ocean and northwest Australian regions (DiNezio et al., 2016; DiNezio & Tierney, 2013; Du et al., 2021). At the same time, reduced ITF transport during low glacial sea level would have reinforced the influence of the Walker circulation by modifying the moisture and heat reaching northwest Australia. From 1,625 to ∼1,300 ka, glacial sea levels ranged from - 50 to - 85 m (Berends et al., 2021 and references therein), therefore substantial change in the land-sea configuration could have led to glacial-interglacial variation in the Walker circulation, the ITF transport and northwest Australian precipitation, which is generally reflected in our records. The second mechanism by which precipitation is affected by the Walker circulation and the ITF is related to obliquity-driven changes in the tilt or depth of the EEP thermocline through the Plio-Pleistocene (Lawrence et al., 2006). In this hypothesis, high (low) obliquity is related to a deep (shallow) thermocline and warm (cool) EEP SSTs, resulting in a weaker (stronger) Walker circulation and ITF and consequently in reduced (enhanced) convection (rainfall) over Maritime Continent and north Australia (Feng et al., 2018; Lawrence et al., 2006). This Pacific dynamical mechanism is opposite to our observations and therefore is likely to be outpaced by the first (sea level-Maritime continent exposure) mechanism; we conclude that obliquity-paced precipitation in the northwest Australian region was primarily governed by the regional processes regulated by sea level changes.

The third mechanism that may explain variations in northwest Australian precipitation is associated with the latitudinal migration of the ITCZ. Obliquity forcing may have played a critical role in driving the south-north migration of the West Pacific ITCZ and modulating the precipitation pattern in the tropical Pacific during the late Quaternary (Liu et al., 2015; Zhang et al., 2020). Site U1483 is located at the southern margin of the modern Indo-Pacific ITCZ where rainfall is sensitive to its latitudinal migration. The cross-hemispherical thermal pressure contrast between the Siberian High and the Australian Low was likely primarily driven by obliquity forcing, with high obliquity leading to strong cross-equatorial northerly winds that pushed the ITCZ south during the late Pleistocene (Liu et al., 2015). This could have strengthened the Australian summer monsoon through the across-equatorial "pressure-push" process in the coupled East Asian–Australian circulation system (An, 2000; Liu et al., 2015). The terrigenous records at Site U1483 are generally consistent with the notion that intensified rainfall occurred at high obliquity due to the southward migration of the ITCZ and enhanced Australian summer monsoon.

In summary, the glacial-interglacial obliquity signal in precipitation in northwest Australia from 1,625 to ∼1,300 ka is likely associated with changes in the Walker circulation and the ITF driven by sea level changes, possibly combined with the latitudinal migrations of the ITCZ. In this study, we are not able to distinguish those two mechanisms. To further understand ITCZ 40 kyr variations across the Indo-Pacific region will require reconstructions of spatial patterns using multiple sites. It is not clear how to explain the evolution of the phase relationship between the precipitation proxies and obliquity forcing (including the lead of precipitation over obliquity maximum between 1,600–1,350 ka (Figure S16 in Supporting Information S1)); perhaps it results from the combination of different mechanisms mentioned above and/or related to the inherent errors (4–6 ka) of the LR04 age model (Lisiecki & Raymo, 2005).

5.3.2. Terrigenous Input Precession-Band Variability

At Site U1483, terrigenous input records (inferred by K wt% and Log ((Al + K + Ti + Fe)/Ca)) exhibit precessional band (19–23 kyr) variance from ∼2,000 to ∼1,300 ka, which becomes stronger and coherent with precessional forcing after 1,625 ka (Figures 4 and 5). Between 1,625 and 1,300 ka, terrigenous input proxies lag precession minimum by ∼1–2 kyr (Figure 6) and are therefore almost out of phase with local summer insolation

(Jan–Feb_20S) and in phase with boreal summer insolation (Jul–Aug_10N) (Figure 6 and Figure S17 in Supporting Information S1), consistent with the precipitation precessional variation over the last 1,600 ka from the same site (Gong et al., 2023; Zhang et al., 2020). This high coherence and phase relationship indicate that instead of being governed by local summer insolation, precipitation in the northwest Australian region was strongly coupled to NH tropical dynamics at precession band in the 40 kyr world. We investigate three plausible underlying mechanisms causing the precession-paced variability in northwest Australian precipitation and terrigenous flux: (a) expansion and contraction of the ITCZ; (b) Walker circulation variability; (c) Indian Ocean Dipole (IOD) dynamics.

The first mechanism that may explain the precessional signal in northwest Australian precipitation is associated with the ITCZ dynamics. Although local insolation directly affects the local land-ocean thermal contrasts and the intensity of the ITCZ, the fact that precessional variability in U1483 precipitation proxy records is out of phase with local insolation indicates that this process was not the primary factor in controlling the rainfall pattern in this region. Instead, based on the above discussions, precipitation in northwest Australia is sensitive to the latitudinal migration of the ITCZ which is sensitive to hemispheric contrasts in temperature and pressure. As such, based on the in-phase precipitation pattern between the two hemispheres, Zhang et al. (2020) point out that the precessional cyclicity in terrigenous discharge at Site U1483 was driven by the contraction and expansion of the ITCZ regulated by precession forcing over the last 410 kyr, supported by the modeling study of Singarayer et al. (2017). The modeling results suggest that the marine ITCZ displays expansion and contraction with precessional cyclicity in response to the interhemispheric temperature gradients during the late Quaternary (Singarayer et al., 2017). During weak precession, when boreal summer is warmer and boreal winter is cooler, increased interhemispheric temperature gradients cause the ITCZ to move further north during the boreal summer and further south during the boreal winter, leading to the expansion of the rain belt and vice versa. This is in agreement with our results, which show enhanced precipitation at the southern margin of the ITCZ (Site U1483) during minimum precession. Due to the limit of ^{230}Th dating, there is no cave stalagmite record with an independent age model in the mid-early Pleistocene, thus we could not further test whether the idea of Zhang et al. (2020) applies to the 40 kyr world. Additional precipitation records from the northern margin and heart of the ITCZ/warm pool during the 40 kyr world will help to test this idea. In summary, based on available information, precessional variability in our terrigenous input records from 1,625 to ∼1,300 ka is potentially due to the expansion and contraction of the ITCZ.

The second possible mechanism causing the observed precessional variance in precipitation records at Site U1483 is related to insolation-forced changes in the Walker circulation. We concur with the previous interpretation that processionally driven changes in warm pool heat storage and the Walker circulation was likely to regulate the terrigenous input variability from 1,625 to ∼1,300 ka (Gong et al., 2023). At precession minima, summer (boreal) solstice occurs at perihelion (maximum Jul-Aug insolation in the tropics), corresponding to warm NH summers and warm SH winters, and the warm pool warms and expands, possibly leading to increased zonal upper thermal contrast and enhanced Walker circulation (La Niña-like). Therefore, increased precipitation should occur at precession minima in the west warm pool, including the northwest Australian region. In fact, Jian et al. (2022) found that the upper ocean heat content of the IPWP exhibited pronounced precession cycles and the maximum heat storage lagged precession minima by ∼3 kyr during the 100 kyr world and attributed their observations to stronger Walker circulation occurring at precession minima driven due to increased upper ocean heat content of the IPWP (Jian et al., 2022). This idea is further supported by observations of precession-minima-associated deeper thermocline in the western equatorial Pacific in the late Quaternary (Lo et al., 2022). We find that precipitation variability in the 100 kyr world at Site U1483 (Zhang et al., 2020) has the same precessional variability and phase relative to insolation compared to our records from the 40 kyr world (Figure 6 and Figure S17 in Supporting Information S1); thus, precessional changes in the Walker circulation documented in the 100 kyr world (Jian et al., 2022; Lo et al., 2022) may also explain precession-paced variability in precipitation during the 40 kyr world.

The third mechanism relevant to precipitation variability at Site U1483 is related to the Indian Ocean Dipole (IOD) dynamics, which influence the hydroclimate in the eastern Indian Ocean and the Timor Sea. A previous modeling study indicates that the frequency and amplitude of the positive phase of the IOD is driven by the solar insolation of the north tropical region and is proportional to the seasonality in the mid-Holocene (Iwakiri & Watanabe, 2019). In this context, at precession minima, NH seasonality is strong, leading to strong positive IOD in boreal summer and drought in the east Indian Ocean, which is the opposite of our precipitation records at Site

U1483. Thus, precessional variation in our records is not likely to be driven by changes in the IOD. However, IOD evolution is poorly understood in the 40 kyr world due to the lack of records and model simulations in the Indian Ocean. In summary, we conclude that the dominant precession variance in precipitation at Site U1483 from 1,625 to ~1,300 ka is likely induced by the expansion (contraction) of the ITCZ and/or the precession-regulated Walker circulation.

Moreover, although it is known that Australian summer monsoon is impacted by the Asian monsoon system, we do not discuss the phase relationship between Asian winter monsoon and our records in this study because the available orbitally-resolved Asian monsoon records are tuned to the orbital template when building the age model (Sun et al., 2006). However, it is worth pointing out that the available EAWM record does show similar orbital cyclicity and some coherence with our terrigenous input proxy both on obliquity and precession bands from ~1,600 to ~1,300 ka (Figures S11 and S18 in Supporting Information S1). We note that the striking decrease in terrigenous input occurred at ~1,640–1,625 ka at Site U1483 during the transition from glacial_58 (MIS 58) to interglacial_57 (MIS 57); this corresponds to the shift from one major glacial loess horizon (L24) to an interglacial paleosol horizon (S23), associated with reduced Asian winter monsoon during deglaciation on orbital timescale (Ding et al., 2002; Sun et al., 2006, 2019).

5.3.3. Productivity Obliquity-Band Variability

At Site U1483, productivity (TN wt%) and bottom water oxygen (U and Log (Mn/S)) proxies show pronounced power concentrated at the obliquity band from 1,625 to ~1,300 ka (Figure 4); the records are strongly coherent with obliquity forcing and benthic $\delta^{18}O$, with productivity minima lagging $\delta^{18}O_{min}$ by ~1.6–2.7 kyr (Figures 5 and 6). From 1,625 to ~1,300 ka, high productivity and low bottom water oxygen characterized glacial periods and vice versa (Figures 3a–3e and Figure S16 in Supporting Information S1). We attribute the glacial-interglacial variations in local productivity to changes in upwelling strength, which could be driven by the intensity of the ITF regulated by sea level changes and/or the strength of the Australian offshore winter monsoon. During glacial times, lower sea level and weak Walker circulation resulted in reduced ITF transport (DiNezio et al., 2011, 2016), leading to reduced stratification of the upper ocean in the Timor Sea and thus increased upwelling and productivity. The alternative mechanism is associated with the Australian winter monsoon, the offshore wind enhanced by the easterly trade winds. Productivity variability lags obliquity forcing and is nearly in phase with $\delta^{18}O$, suggesting that it is likely ultimately tied to global glacial-interglacial changes, rather than regional processes alone. During glacial times, changes in the large-scale atmospheric circulation caused strong Australian winter monsoon, which could induce enhanced coastal upwelling in the northwest Australian region and therefore high glacial productivity (Gong et al., 2023). We cannot distinguish between those two mechanisms (ITF vs. wind-induced upwelling) in this study: both are tightly linked to glacial/interglacial changes as reflected in the benthic $\delta^{18}O$ signal and could reinforce each other. Moreover, similar obliquity variation and phasing have been reported at EEP Site 846 during this time, which has been attributed to changes in the tilt or depth of the EEP thermocline in response to obliquity forcing (Lawrence et al., 2006). Since shallow subsurface water at Site U1483 is mainly derived from the Pacific, including North Pacific upper waters and AAIW, we think the variations in the nutrient content in the source water probably could have reinforced productivity changes driven by the upwelling strength, but likely had a minor effect and needs further studies to verify. In summary, at Site U1483, obliquity-paced variability in productivity is strongly coherent and nearly in-phase relationship with the $\delta^{18}O$ signal suggesting that productivity variability in the Timor Sea was driven by the changes in intensity of the ITF related to sea level changes and/or in the strength of the offshore winds from 1,625 to ~1,300 ka.

5.3.4. Productivity Precession-Band Variability

Productivity (TN wt%) and bottom water oxygenation (U and Log (Mn/S)) proxies at Site U1483 only show precessional variance from 2,000 to 1,625 ka, similar to the behavior of benthic $\delta^{18}O$ (Figure 4). Specifically, from ~1,900 to 1,700 ka, benthic $\delta^{18}O$, productivity and oxygenation proxies exhibit strong coherence with precession (Figure 5), with productivity (TN wt%) lagging benthic $\delta^{18}O$ by 1.8 ($\pm$1.8) kyr. This coupling between productivity/oxygenation proxies and benthic $\delta^{18}O$ is similar to what was found in the obliquity band, suggesting that the precession signal in productivity was likely controlled by the intensity of the ITF regulated by sea level changes and/or the strength of the Australian offshore winter monsoon (see Section 5.3.3). Because of the low resolution of available sea level reconstructions during this time interval, it is not possible to resolve precessional variations in sea level change though there seems to be orbital band variations between 2,000 and

1,700 ka (Rohling et al., 2014). For this reason, we rely on the benthic $\delta^{18}O$ record as an adequate reflection of global climate and sea level variability, and thus our results showing a shift in productivity at Site U1483, from a dominant precession periodicity to a dominant obliquity periodicity at ~1,625 ka, was strongly linked to a shift in periodicity in global ice volume changes and its influence on the strength of the ITF.

5.3.5. Change in Climate Sensitivity During the Mid-Early Pleistocene

As discussed above, the variability in terrigenous input and productivity at Site U1483 reveals a significant transition period such that more power was concentrated at orbital bands and was more coherent with orbital forcing after ~1,650 ka (Figures 4 and 5). In the obliquity band, the increase in sensitivity and coherence from ~1,800 to ~1,600 ka observed in our productivity and bottom oxygen records has also been observed in globally widespread records (deMenocal, 1995; Lawrence et al., 2006; Li et al., 2011; Martinez-Garcia et al., 2010; Peterson et al., 2020). To explain the increase in sensitivity to obliquity forcing, previous studies proposed that orbital-scale pCO_2 change likely played a major role to coordinate the response of tropical climate to high-latitude forcing, potentially through coupling with the enhanced iron fertilization-CO_2 feedback due to increased subantarctic iron deposition (Herbert et al., 2010; Lawrence et al., 2006; Martínez-Garcia et al., 2011; Peterson et al., 2020). Atmospheric pCO_2 feedbacks likely amplify the climatic response to obliquity forcing as global ice expanded, resulting in a higher sensitivity of the climate system to obliquity forcing. The recent published modeling-reconstructed pCO_2 record shows strong obliquity band variance and coherence starting at ~1,600 ka (Berends et al., 2021) (Figure 5), supporting the proposed global greenhouse gas forcing mechanism.

At the precession band, different from the behavior of benthic $\delta^{18}O$ and modeling-reconstructed pCO_2 (Berends et al., 2021) (Figure 5), our terrigenous input proxies show pronounced coherence to precession after ~1,650 ka. We attribute this to local feedbacks (e.g., Walker circulation) that amplified precession variance in the precipitation records. It is known that a major reorganization occurred in the tropical oceans between 1,800 and 1,600 ka with development of strong Walker circulation accompanied by shoaling of the thermocline (Ravelo et al., 2004). The change of the mean state may have affected the strength of local feedbacks that amplified small perturbations in the solar forcing. For example, if the mean depth of the thermocline were shallower, solar forcing could more readily affect the Walker circulation, resulting in precession band variance in precipitation records.

Taken together, the striking appearance of 41 kyr obliquity cycles at ~1,650 ka in our productivity and oxygen records supports the notion that pCO_2 likely played a major role in driving obliquity-band climatic variations in the mid-early Pleistocene. The increased coherence to precession in our terrigenous input proxies after ~1,650 ka is likely a result of local feedbacks.

5.4. Nitrogen Isotope Variability

Based on the results of $\delta^{13}C_{org}$ and TOC:TN ratios (see Section 4.1.4), the organic matter at Site U1483 is primarily of marine origin with little terrestrial and inorganic N influences, and thus we attribute variability in bulk $\delta^{15}N$ values to be primarily driven by marine processes. Site U1483 is located in a relatively oligotrophic region, where surface nitrate is completely consumed on an annual basis. The source of surface nitrate is mainly from the thermocline water that flows into the Timor Sea as part of the ITF, upwells due to monsoonal winds (Alongi et al., 2011), and is completely utilized. Therefore, $\delta^{15}N$ of organic matter in the sediment (bulk $\delta^{15}N$) at Site U1483 should be primarily controlled by the thermocline source water process (upwelled nitrate) instead of the local primary production. However, a previous study found that lower bulk $\delta^{15}N$ occurred when local productivity was high during the LGM and proposed that bulk $\delta^{15}N$ in the Timor Throughflow could reflect glacial-interglacial changes in nitrogen utilization and potentially N_2 fixation (Müller & Opdyke, 2000). Thus, we investigate the influences of both changes in source water and changes in local productivity on bulk $\delta^{15}N$ at Site U1483 over the last 2,000 ka.

On long timescales, bulk $\delta^{15}N$ at Site U1483 exhibits no pronounced secular trend over the last 2,000 ka and no significant transition between 1,700 and 1,400 ka, when productivity started to shift to lower values (Figure 2g, Table 1); therefore, trends in bulk $\delta^{15}N$ are decoupled from trends in productivity. This is different from observations at EEP Sites 1,239 and 1,240, which show that the productivity shift at ~1,600 ka is coupled to a shift in bulk $\delta^{15}N$ (Etourneau et al., 2013), suggesting local nitrate utilization is an important factor in driving bulk $\delta^{15}N$ in the EEP but not at Site U1483. Instead, the secular long-term trend in bulk $\delta^{15}N$ at Site U1483 reflects changes

in the source thermocline water. This is supported by the fact that Site U1483 exhibits similar trends to the bulk $\delta^{15}N$ records from distant Site 1,012 (located in the California margin) over the last ~2,000 kyr (Figure 2g) and from Site U1486 (located in the Bismarck Sea north of New Guinea) over the last ~1,400 ka (Lambert et al., 2022). Since the upper thermocline waters in the Timor Sea are mostly sourced from the North Pacific (Talley & Sprintall, 2005), this result indicates that bulk $\delta^{15}N$ at Site U1483 is controlled by the changes in source water over long timescales during the Pleistocene epoch. Bulk $\delta^{15}N$ records from Sites 1,012 and U1486 are reported to primarily reflect denitrification change in the Eastern Tropical Pacific (ETP) oxygen minimum zones (OMZs) during the Pleistocene, as a result of remineralization of organic matter exported from ETP OMZs leading to zonally spreading denitrification signals across the Pacific (Lambert et al., 2022; Liu et al., 2005). Based on the striking similarity in long $\delta^{15}N$ bulk records between Sites U1483 and 1,012, we concur with the interpretation that denitrification signals from ETP are transported westward across the Pacific (Jia & Li, 2011; Lambert et al., 2022), driving the bulk $\delta^{15}N$ variation in the Timor Sea. Notably, there is a general offset of ~1–3‰ in $\delta^{15}N$ values between Sites U1483 (average = 6.5‰), 1012 (average = 7.7‰) and U1486 (average = 9.6‰) over the last ~1,400 kyr; lower bulk $\delta^{15}N$ values at Site U1483 potentially reflect the prevalence of local N_2 fixation in the Timor Sea (Müller & Opdyke, 2000).

Orbital variations in the bulk $\delta^{15}N$ record at Site U1483 generally exhibit different spectral power features and correlations with TN wt% from 2,000 to 1,300 ka (Figure S19 in Supporting Information S1), although there are some intervals that indicate coherent variability and therefore potentially some local controls of productivity on bulk $\delta^{15}N$. Between 2,000 and 1,625 ka, bulk $\delta^{15}N$ shows significant negative correlation with productivity (oxygen) proxies (Figure S17 in Supporting Information S1, Table 2) and high coherence with the productivity index (TN wt%) at the 19–23 kyr (precession) band from ~1,650 to 1,750 ka and at ~1,850 ka (Figure S20 in Supporting Information S1). During those specific time intervals, lower $\delta^{15}N$ occurs during higher productivity periods, indicating changes in local N utilization likely leading to the precessional variations in bulk $\delta^{15}N$ records, probably related to precession-driven sea level changes. After ~1,750 ka, bulk $\delta^{15}N$ at Site U1483 shows high coherence with bulk $\delta^{15}N$ at Site 1,012 both at the 41 kyr (obliquity) and 19–23 kyr (precession) bands and little coherence (and correlation) with productivity index (TN wt%) (Figures S19 and S20 in Supporting Information S1, Table 2), suggesting that bulk $\delta^{15}N$ variation at Site U1483 is dominated by source water processes during this period. Liu et al. (2005) attributed the obliquity variation in bulk $\delta^{15}N$ and SST at Site 1,012 to high latitude forcing modulation of thermocline conditions, including the strength of denitrification, throughout the Plio-Pleistocene. Diz and Pérez-Arlucea (2021) proposed that 41 kyr glacial-interglacial variability in bulk $\delta^{15}N$ record records from OMZs during the middle Pleistocene is caused by enhanced glacial ventilation of tropical thermocline due to increased AAIW influence. In terms of the precessional variability, previous proxy and modeling studies indicated that precession has a strong impact on tropical Pacific thermocline depth and upwelling strength (Clement et al., 1999; Rafter & Charles, 2012), which could lead to the 19–23 kyr signals observed in denitrification records (Kong et al., 2021; Lacerra et al., 2021). We note that the bulk $\delta^{15}N$ record at Site U1483 does not exhibit the relatively high peak values that appear in the 1,012 record (e.g., ~1,430 ka, ~1,560 ka) (Figure 2g). The differences in amplitudes and peak values between those two records could be related to the modification of source water while transferring from the Pacific to the Timor Sea and/or associated with offsetting local denitrification isotopic effects.

In summary, our results reveal striking similarities in bulk $\delta^{15}N$ records between Sites U1483 and 1012, suggesting that bulk $\delta^{15}N$ in the Timor Sea was primarily driven by changes in the source water from the North Pacific at orbital and longer timescales, reflecting denitrification changes in the ETP. In some specific intervals, orbital variations in bulk $\delta^{15}N$ at Site U1483 also likely reflect changes in local N utilization.

5.5. Benthic Carbon Isotope Interpretation

In some cases, changes in surface productivity can be monitored by changes in deep ocean chemistry such as benthic $\delta^{13}C$, which would be expected to decrease during times of stronger organic matter export from the surface water and remineralization at depth. However, benthic $\delta^{13}C$ is also influenced by whole ocean changes in seawater $\delta^{13}C$ values and by deep water mass mixing. At Site U1483, benthic $\delta^{13}C$ shows significant variance in the obliquity band (41 kyr) from 1,625 to 1,300 ka, and weak precessional variance (19–23 kyr) from 2,000 to 1,625 ka (Figure S11 in Supporting Information S1). Benthic $\delta^{13}C$ exhibits similar behaviors to benthic $\delta^{18}O$ and it is strongly coherent with benthic $\delta^{18}O$ both at the obliquity and precession bands from 2,000 to 1,300 ka

(Figure 5). Benthic $\delta^{13}C$ also shows strong correlation with U concentration at the obliquity band from 2,000 to 1,300 ka (Figure S10 in Supporting Information S1). To understand if these observations are related to global rather than local effects, the benthic $\delta^{13}C$ record from Site U1483 is compared to that from ODP Site 849, which is a deep site (>3,800 m) located in the east equatorial Pacific, representing mean Pacific Ocean $\delta^{13}C$ values (Lyle et al., 2019 (updated age model); Mix et al., 1995). These two records show striking similarities in absolute values and orbital variations (Figure S10 in Supporting Information S1). Bottom water at Site U1483 (~1,700 m) is likely derived from the AAIW from the South Pacific and potentially influenced by the Indian Deep Water (Tomczak & Godfrey, 2003). The consistency between the benthic $\delta^{13}C$ records from the two sites suggests that benthic $\delta^{13}C$ at Site U1483 primarily reflects whole ocean changes as represented by deep Pacific Site 849 at orbital and longer timescales in the mid-early Pleistocene. This is also reflected in the pronounced decoupling between productivity (TN MAR) and bottom oxygen proxies (U and Log (Mn/S)) from 1,700 to 1,650 ka (Figure S10 in Supporting Information S1), when bottom water oxygenation and benthic $\delta^{13}C$ are governed by source water signals instead of local productivity. However, specifically during interglacials before ~1,600 ka, benthic $\delta^{13}C$ at Site U1483 shows relatively higher values than that at Site 849 (Figure S10 in Supporting Information S1). This interglacial offset indicates local processes may play a role in modifying the benthic $\delta^{13}C$ at Site U1483 before ~1,600 ka, potentially related to changes in deep water circulation leading to better ventilation in the Timor Sea.

6. Conclusions

We provide multiproxy reconstructions from Site U1483 to investigate hydroclimate and productivity changes in the Timor Sea (off northwest Australia) during the 40 kyr world of the mid-early Pleistocene. On the long-term, the decrease in terrigenous input from ~1,700 to ~1,400 ka indicates increased aridification in the northwest Australian region. We argue that the restriction of the ITF due to lower glacial sea level and Asian monsoon feedbacks, combined with the contraction of the IPWP, reduced moisture supply and precipitation to northwest Australia, leading to aridification and reduced terrigenous flux from ~1,700 to ~1,400 ka. Productivity in the Timor Sea shifted to lower values during the transition from ~1,700 to ~1,400 ka, showing similarities to the trend at EEP Site 846. We conclude that the decline in productivity at Site U1483 reflects a decrease in nutrient supply from Pacific source waters, associated with nutrient redistribution in the global ocean at this time. On orbital timescales, our records reveal a significant transition in the sensitivity of the U1483 proxy records to orbital forcing after ~1,650 ka; orbital-scale pCO_2 changes and local feedbacks are likely to play important roles in driving obliquity- and precession-paced climatic variations. Terrigenous input proxy records (reflecting precipitation) at Site U1483 only show weak coherency with obliquity forcing from 1,625 to ~1,300 ka. We conclude that the glacial-interglacial obliquity-paced precipitation in northwest Australia is likely associated with changes in the Walker circulation and the ITF regulated by sea level exposure of the Maritime continent, possibly combined with the latitudinal migrations of the ITCZ. At the precession band, terrigenous input records are strongly coherent with precession and are almost out of phase with local summer insolation from ~1,650 to ~1,300 ka. We attribute the precession-paced variability in precipitation to the expansion and contraction of the ITCZ and/or the precession-regulated changes in the Walker circulation. Orbitally-modulated variations in productivity (oxygen) in the Timor Sea are coherent with and nearly in-phase with the benthic $\delta^{18}O$ signal from 2,000 to 1,300 ka, with a shift from dominant precessional periodicity to dominant obliquity periodicity at ~1,650 ka. Our results reveal that productivity variability in the Timor Sea was strongly linked to global ice volume changes, driven by changes in ITF intensity related to sea level changes and/or in the strength of offshore winds. The striking similarities in bulk $\delta^{15}N$ records between Sites U1483 and 1,012 indicate that changes in Pacific source water are the primary control on biogeochemical changes in the Timor Sea at orbital and longer timescales in the mid-early Pleistocene. This study offers new insights on hydroclimate and productivity evolution in northwest Australia and extends the history of ITF variability and Australian monsoon dynamics into the 40 kyr world of the mid-early Pleistocene.

Conflict of Interest

The authors declare no conflicts of interest relevant to this study.

Data Availability Statement

Data associated with this study are archived at National Oceanic and Atmospheric Administration (NOAA) (Zhang et al., 2023).

Acknowledgments
We thank Colin Carney for analytical assistance, Sarah White, Michelle Drake, Kimberly DeLong, Elly Wash, and Eve Pugsley for helpful conversions and feedback on earlier version of the manuscript. We also thank Dr. Zhaojie Yu and another anonymous reviewer for their helpful comments and suggestions that improved the manuscript. This research used samples and data provided by the International Ocean Discovery Program. Funding was provided by American Chemical Society (ACS) Grant 61090-ND8 and United States Science Support Program (USSSP) National Science Foundation (NSF) Grant 1736686. Y.Z. acknowledges financial support from the China Scholarship Council (CSC).

References

Alongi, D. M., Edyvane, K., do Ceu Guterres, M. O., Pranowo, W. S., Wirasantosa, S., & Wasson, R. (2011). Biophysical profile of the Arafura and Timor seas. In *Report prepared for the Arafura Timor seas ecosystem action (ATSEA) program* (p. 32).

An, Z. (2000). The history and variability of the East Asian paleomonsoon climate. *Quaternary Science Reviews*, *19*(1–5), 171–187. https://doi.org/10.1016/S0277-3791(99)00060-8

Auer, G., De Vleeschouwer, D., Smith, R. A., Bogus, K., Groeneveld, J., Grunert, P., et al. (2019). Timing and pacing of Indonesian throughflow restriction and its connection to late Pliocene climate shifts. *Paleoceanography and Paleoclimatology*, *34*(4), 635–657. https://doi.org/10.1029/2018PA003512

Bali, H., Gupta, A. K., Mohan, K., Thirumalai, K., Tiwari, S. K., & Panigrahi, M. K. (2020). Evolution of the oligotrophic West Pacific warm pool during the Pliocene-Pleistocene boundary. *Paleoceanography and Paleoclimatology*, *35*(11), e2020PA003875. https://doi.org/10.1029/2020PA003875

Beaufort, L., van der Kaars, S., Bassinot, F. C., & Moron, V. (2010). Past dynamics of the Australian monsoon: Precession, phase and links to the global monsoon concept. *Climate of the Past*, *6*(5), 695–706. https://doi.org/10.5194/cp-6-695-2010

Beck, J. W., Zhou, W., Li, C., Wu, Z., White, L., Xian, F., et al. (2018). A 550,000-year record of East Asian monsoon rainfall from ^{10}Be in loess. *Science*, *360*(6391), 877–881. https://doi.org/10.1126/science.aam5825

Berends, C. J., de Boer, B., & van de Wal, R. S. W. (2021). Reconstructing the evolution of ice sheets, sea level, and atmospheric CO_2 during the past 3.6 million years. *Climate of the Past*, *17*(1), 361–377. https://doi.org/10.5194/cp-17-361-2021

Berner, N., Trauth, M. H., & Holschneider, M. (2022). Bayesian inference about Plio-Pleistocene climate transitions in Africa. *Quaternary Science Reviews*, *277*, 107287. https://doi.org/10.1016/j.quascirev.2021.107287

Boyer, T. P., Garcia, H. E., Locarnini, R. A., Zweng, M. M., Alexey, V., Reagan, J. R., et al. (2018). World ocean atlas 2018 (temperature and salinity). Retrieved from https://www.ncei.noaa.gov/archive/accession/NCEI-WOA18

Brierley, C. M., Fedorov, A. V., Liu, Z., Herbert, T. D., Lawrence, K. T., & LaRiviere, J. P. (2009). Greatly expanded tropical warm pool and weakened Hadley circulation in the early Pliocene. *Science*, *323*(5922), 1714–1718. https://doi.org/10.1126/science.1167625

Burls, N. J., & Fedorov, A. V. (2017). Wetter subtropics in a warmer world: Contrasting past and future hydrological cycles. *Proceedings of the National Academy of Sciences of the United States of America*, *114*(49), 12888–12893. https://doi.org/10.1073/pnas.1703421114

Chang, C.-P., Wang, Z., & Hendon, H. (2006). The Asian winter monsoon. In *The Asian monsoon* (pp. 89–127). Springer Berlin Heidelberg. https://doi.org/10.1007/3-540-37722-0_3

Chen, X. Y., & Barton, C. E. (1991). Onset of aridity and dune-building in central Australia: Sedimentological and magnetostratigraphic evidence from Lake Amadeus. *Palaeogeography, Palaeoclimatology, Palaeoecology*, *84*(1–4), 55–73. https://doi.org/10.1016/0031-0182(91)90035-P

Chen, Y., Xu, J., Liu, J., Li, T., Xiong, Z., Zhang, P., & Yan, H. (2022). Climatic and tectonic constraints on the Plio–Pleistocene evolution of the Indonesian Throughflow intermediate water recorded by benthic δ^{18}O from IODP site U1482. *Quaternary Science Reviews*, *295*, 107666. https://doi.org/10.1016/j.quascirev.2022.107666

Christensen, B. A., Renema, W., Henderiks, J., De Vleeschouwer, D., Groeneveld, J., Castañeda, I. S., et al. (2017). Indonesian Throughflow drove Australian climate from humid Pliocene to arid Pleistocene. *Geophysical Research Letters*, *44*(13), 6914–6925. https://doi.org/10.1002/2017GL072977

Clement, A. C., Seager, R., & Cane, M. A. (1999). Orbital controls on the El Niño/Southern Oscillation and the tropical climate. *Paleoceanography*, *14*(4), 441–456. https://doi.org/10.1029/1999PA900013

Connock, G. T., Owens, J. D., & Liu, X.-L. (2022). Biotic induction and microbial ecological dynamics of Oceanic Anoxic Event 2. *Communications Earth & Environment*, *3*(1), 136. https://doi.org/10.1038/s43247-022-00466-x

Cortese, G., & Gersonde, R. (2008). Plio/Pleistocene changes in the main biogenic silica carrier in the Southern Ocean, Atlantic Sector. *Marine Geology*, *252*(3–4), 100–110. https://doi.org/10.1016/j.margeo.2008.03.015

Cortese, G., Gersonde, R., Hillenbrand, C.-D., & Kuhn, G. (2004). Opal sedimentation shifts in the World Ocean over the last 15 Myr. *Earth and Planetary Science Letters*, *224*(3–4), 509–527. https://doi.org/10.1016/j.epsl.2004.05.035

Dang, H., Wu, J., Xiong, Z., Qiao, P., Li, T., & Jian, Z. (2020). Orbital and sea-level changes regulate the iron-associated sediment supplies from Papua New Guinea to the equatorial Pacific. *Quaternary Science Reviews*, *239*, 106361. https://doi.org/10.1016/j.quascirev.2020.106361

De Deckker, P., Barrows, T. T., & Rogers, J. (2014). Land–sea correlations in the Australian region: Post-glacial onset of the monsoon in northwestern Western Australia. *Quaternary Science Reviews*, *105*, 181–194. https://doi.org/10.1016/j.quascirev.2014.09.030

de Menocal, P. B. (1995). Plio-pleistocene African climate. *Science*, *270*(5233), 53–59. https://doi.org/10.1126/science.270.5233.53

De Vleeschouwer, D. (2017). Natural gamma radiation-derived K, U and Th contents of marine sediments obtained during IODP expeditions with DV JOIDES resolution [Dataset]. Interdisciplinary Earth Data Alliance (IEDA). https://doi.org/10.1594/IEDA/100668

DiNezio, P. N., Clement, A., Vecchi, G. A., Soden, B., Broccoli, A. J., Otto-Bliesner, B. L., & Braconnot, P. (2011). The response of the walker circulation to Last Glacial Maximum forcing: Implications for detection in proxies: LGM walker circulation. *Paleoceanography*, *26*(3), PA3217. https://doi.org/10.1029/2010PA002083

DiNezio, P. N., & Tierney, J. E. (2013). The effect of sea level on glacial Indo-Pacific climate. *Nature Geoscience*, *6*(6), 485–491. https://doi.org/10.1038/ngeo1823

DiNezio, P. N., Timmermann, A., Tierney, J. E., Jin, F., Otto-Bliesner, B., Rosenbloom, N., et al. (2016). The climate response of the Indo-Pacific warm pool to glacial sea level. *Paleoceanography*, *31*(6), 866–894. https://doi.org/10.1002/2015PA002890

Ding, Z. L., Derbyshire, E., Yang, S. L., Yu, Z. W., Xiong, S. F., & Liu, T. S. (2002). Stacked 2.6-Ma grain size record from the Chinese loess based on five sections and correlation with the deep-sea δ^{18}O record: Stacked quaternary climate record from Chinese loess. *Paleoceanography*, *17*(3), 5-1–5-21. https://doi.org/10.1029/2001PA000725

Diz, P., & Pérez-Arlucea, M. (2021). Southern Ocean sourced waters modulate eastern equatorial pacific denitrification during the mid-Pleistocene transition. *Palaeogeography, Palaeoclimatology, Palaeoecology*, *577*, 110531. https://doi.org/10.1016/j.palaeo.2021.110531

Du, X., Russell, J. M., Liu, Z., Otto-Bliesner, B. L., Gao, Y., Zhu, C., et al. (2021). Deglacial trends in Indo-Pacific warm pool hydroclimate in an isotope-enabled Earth system model and implications for isotope-based paleoclimate reconstructions. *Quaternary Science Reviews*, *270*, 107188. https://doi.org/10.1016/j.quascirev.2021.107188

Ehrenberg, S., & Svånå, T. A. (2001). Use of spectral gamma-ray signature to interpret stratigraphic surfaces in carbonate strata: An example from the Finnmark carbonate platform (Carboniferous-Permian). *Marine Pollution Bulletin*, *9*(3), 63. https://doi.org/10.1016/0025-326X(78)90448-4

Etourneau, J., Martinez, P., Blanz, T., & Schneider, R. (2009). Pliocene–Pleistocene variability of upwelling activity, productivity, and nutrient cycling in the Benguela region. *Geology*, *37*(10), 871–874. https://doi.org/10.1130/G25733A.1

Etourneau, J., Robinson, R. S., Martinez, P., & Schneider, R. (2013). Equatorial Pacific peak in biological production regulated by nutrient and upwelling during the late Pliocene/early Pleistocene cooling. *Biogeosciences*, *10*(8), 5663–5670. https://doi.org/10.5194/bg-10-5663-2013

Fang, X., An, Z., Clemens, S. C., Zan, J., Shi, Z., Yang, S., & Han, W. (2020). The 3.6-Ma aridity and westerlies history over midlatitude Asia linked with global climatic cooling. *Proceedings of the National Academy of Sciences of the United States of America*, *117*(40), 24729–24734. https://doi.org/10.1073/pnas.1922710117

Fedorov, A. V., Burls, N. J., Lawrence, K. T., & Peterson, L. C. (2015). Tightly linked zonal and meridional sea surface temperature gradients over the past five million years. *Nature Geoscience*, *8*(12), 975–980. https://doi.org/10.1038/ngeo2577

Feng, M., Zhang, N., Liu, Q., & Wijffels, S. (2018). The Indonesian throughflow, its variability and centennial change. *Geoscience Letters*, *5*(1), 3. https://doi.org/10.1186/s40562-018-0102-2

Gallagher, S. J., Wallace, M. W., Li, C. L., Kinna, B., Bye, J. T., Akimoto, K., & Torii, M. (2009). Neogene history of the West Pacific warm pool, Kuroshio and Leeuwin currents: Neogene west Pacific warm pool. *Paleoceanography*, *24*(1), PA1206. https://doi.org/10.1029/2008pa001660

Geen, R., Bordoni, S., Battisti, D. S., & Hui, K. (2020). Monsoons, ITCZs, and the concept of the global monsoon. *Reviews of Geophysics*, *58*(4), e2020RG000700. https://doi.org/10.1029/2020RG000700

Gingele, F. X., & De Deckker, P. (2004). Fingerprinting Australia's rivers with clay minerals and the application for the marine record of climate change. *Australian Journal of Earth Sciences*, *51*(3), 339–348. https://doi.org/10.1111/j.1400-0952.2004.01061.x

Gong, L., Holbourn, A., Kuhnt, W., Opdyke, B., Zhang, Y., Ravelo, A. C., et al. (2023). Middle Pleistocene re-organization of Australian monsoon. *Nature Communications*, *14*(1), 2002. https://doi.org/10.1038/s41467-023-37639-x

Gordon, A. L., & Fine, R. A. (1996). Pathways of water between the Pacific and Indian oceans in the Indonesian seas. *Nature*, *379*(6561), 146–149. https://doi.org/10.1038/379146a0

Gordon, A. L., Susanto, R. D., & Vranes, K. (2003). Cool Indonesian throughflow as a consequence of restricted surface layer flow. *Nature*, *425*(6960), 824–828. https://doi.org/10.1038/nature02038

Hammer, Ø., Harper, D. A. T., & Ryan, P. D. (2001). PAST: Paleontological statistics software package for education and data analysis. *Palaeontologia Electronica*, *4*(1), 9.

Harris, P. G., Zhao, M., Rosell-Melé, A., Tiedemann, R., Sarnthein, M., & Maxwell, J. R. (1996). Chlorin accumulation rate as a proxy for Quaternary marine primary productivity. *Nature*, *383*(6595), 63–65. https://doi.org/10.1038/383063a0

He, Y., Wang, H., & Liu, Z. (2021). Development of the Leeuwin current on the northwest shelf of Australia through the Pliocene-Pleistocene period. *Earth and Planetary Science Letters*, *559*, 116767. https://doi.org/10.1016/j.epsl.2021.116767

Heidemann, H., Cowan, T., Henley, B. J., Ribbe, J., Freund, M., & Power, S. (2023). Variability and long-term change in Australian monsoon rainfall: A review. *WIREs Climate Change*, *14*(3). https://doi.org/10.1002/wcc.823

Herbert, T. D., Peterson, L. C., Lawrence, K. T., & Liu, Z. (2010). Tropical ocean temperatures over the past 3.5 million years. *Science*, *328*(5985), 1530–1534. https://doi.org/10.1126/science.1185435

Holbourn, A., Kuhnt, W., Kawamura, H., Jian, Z., Grootes, P., Erlenkeuser, H., & Xu, J. (2005). Orbitally paced paleoproductivity variations in the Timor Sea and Indonesian throughflow variability during the last 460 kyr: Timor Sea paleoproductivity. *Paleoceanography*, *20*(3), PA3002. https://doi.org/10.1029/2004PA001094

Hollstein, M., Mohtadi, M., Rosenthal, Y., Prange, M., Oppo, D. W., Martínez Méndez, G., et al. (2018). Variations in Western Pacific Warm Pool surface and thermocline conditions over the past 110,000 years: Forcing mechanisms and implications for the glacial Walker circulation. *Quaternary Science Reviews*, *201*, 429–445. https://doi.org/10.1016/j.quascirev.2018.10.030

Hopmans, E. C., Weijers, J. W. H., Schefuß, E., Herfort, L., Sinninghe Damsté, J. S., & Schouten, S. (2004). A novel proxy for terrestrial organic matter in sediments based on branched and isoprenoid tetraether lipids. *Earth and Planetary Science Letters*, *224*(1–2), 107–116. https://doi.org/10.1016/j.epsl.2004.05.012

Ishiwa, T., Yokoyama, Y., Reuning, L., McHugh, C. M., De Vleeschouwer, D., & Gallagher, S. J. (2019). Australian Summer Monsoon variability in the past 14,000 years revealed by IODP Expedition 356 sediments. *Progress in Earth and Planetary Science*, *6*(1), 17. https://doi.org/10.1186/s40645-019-0262-5

Iwakiri, T., & Watanabe, M. (2019). Strengthening of the Indian Ocean Dipole with increasing seasonal cycle in the mid-Holocene. *Geophysical Research Letters*, *46*(14), 8320–8328. https://doi.org/10.1029/2019GL083088

Jia, G., & Li, Z. (2011). Easterly denitrification signal and nitrogen fixation feedback documented in the western Pacific sediments: Denitrification record in West Pacific. *Geophysical Research Letters*, *38*(24), L24605. https://doi.org/10.1029/2011GL050021

Jian, Z., Wang, Y., Dang, H., Mohtadi, M., Rosenthal, Y., Lea, D. W., et al. (2022). Warm pool ocean heat content regulates ocean–continent moisture transport. *Nature*, *612*(7938), 92–99. https://doi.org/10.1038/s41586-022-05302-y

Kaboth-Bahr, S., & Mudelsee, M. (2022). The multifaceted history of the walker circulation during the Plio-Pleistocene. *Quaternary Science Reviews*, *286*, 107529. https://doi.org/10.1016/j.quascirev.2022.107529

Kershaw, P., Martin, H. A., & Mason, J. M. (2017). In R. S. Hill (Ed.), *History of the Australian vegetation: Cretaceous to recent*. University of Adelaide Press. Reprint. https://doi.org/10.20851/australian-vegetation

Kershaw, P., Moss, P., & Van Der Kaars, S. (2003). Causes and consequences of long-term climatic variability on the Australian continent: Long term climatic variability. *Freshwater Biology*, *48*(7), 1274–1283. https://doi.org/10.1046/j.1365-2427.2003.01085.x

Kershaw, P., van der Kaars, S., & Moss, P. T. (2003). Late Quaternary Milankovitch-scale climatic change and variability and its impact on monsoonal Australasia. *Marine Geology*, *201*(1–3), 81–95. https://doi.org/10.1016/S0025-3227(03)00210-X

Klinkhammer, G. P., & Palmer, M. R. (1991). Uranium in the oceans: Where it goes and why. *Geochimica et Cosmochimica Acta*, *55*(7), 1799–1806. https://doi.org/10.1016/0016-7037(91)90024-Y

Kong, T., Wang, Y., Sigman, D., Ren, H., & Wang, X. (2021). Revisiting glacial-interglacial changes in pelagic denitrification in the South Pacific (Vol. *2021*). PP34B-10.

Kotov, S., & Pälike, H. (2018). QAnalySeries – A cross-platform time series tuning and analysis tool [other]. *Geology*. https://doi.org/10.1002/essoar.10500226.1

Kuhnt, W., Holbourn, A., Hall, R., Zuvela, M., & Käse, R. (2004). Neogene history of the Indonesian throughflow. In P. Clift, W. Kuhnt, P. Wang, & D. Hayes (Eds.), *Geophysical monograph series* (Vol. 149, pp. 299–320). American Geophysical Union. https://doi.org/10.1029/149GM16

Kuhnt, W., Holbourn, A., Xu, J., Opdyke, B., De Deckker, P., Röhl, U., & Mudelsee, M. (2015). Southern Hemisphere control on Australian monsoon variability during the late deglaciation and Holocene. *Nature Communications*, *6*(1), 5916. https://doi.org/10.1038/ncomms6916

Lacerra, M., Sigman, D., Martinez-Garcia, A., & Haug, G. (2021). A foraminifera-bound nitrogen isotope record from the eastern tropical North Pacific spanning the last glacial-interglacial transition. *2021*, PP41A-03.

Lambert, J. E., Gibson, K. A., Linsley, B. K., Bova, S. C., Rosenthal, Y., & Surprenant, M. (2022). Equatorial Pacific bulk sediment $\delta^{15}N$ supports a secular increase in Southern Ocean nitrate utilization after the mid-Pleistocene Transition. *Quaternary Science Reviews*, *278*, 107348. https://doi.org/10.1016/j.quascirev.2021.107348

Lawrence, K. T., Liu, Z., & Herbert, T. D. (2006). Evolution of the eastern tropical Pacific through Plio-Pleistocene glaciation. *Science*, *312*(5770), 79–83. https://doi.org/10.1126/science.1120395

Li, L., Li, Q., Tian, J., Wang, P., Wang, H., & Liu, Z. (2011). A 4-Ma record of thermal evolution in the tropical western Pacific and its implications on climate change. *Earth and Planetary Science Letters*, *309*(1–2), 10–20. https://doi.org/10.1016/j.epsl.2011.04.016

Liao, S., Liu, X.-L., Manz, K. E., Pennell, K. D., Novak, J., Santos, E., & Huang, Y. (2023). Comprehensive analysis of alkenones by reversed-phase HPLC-MS with unprecedented selectivity, linearity and sensitivity. *Talanta*, *260*, 124653. https://doi.org/10.1016/j.talanta.2023.124653

Lisiecki, L. E., & Raymo, M. E. (2005). A Pliocene-Pleistocene stack of 57 globally distributed benthic $\delta^{18}O$ records: Pliocene-Pleistocene benthic stack. *Paleoceanography*, *20*(1), PA1003. https://doi.org/10.1029/2004PA001071

Liu, Y., Lo, L., Shi, Z., Wei, K.-Y., Chou, C.-J., Chen, Y.-C., et al. (2015). Obliquity pacing of the western Pacific intertropical convergence zone over the past 282,000 years. *Nature Communications*, *6*(1), 10018. https://doi.org/10.1038/ncomms10018

Liu, Z., Altabet, M. A., & Herbert, T. D. (2005). Glacial-interglacial modulation of eastern tropical North Pacific denitrification over the last 1.8-Myr. *Geophysical Research Letters*, *32*(23), L23607. https://doi.org/10.1029/2005GL024439

Liu, Z., Altabet, M. A., & Herbert, T. D. (2008). Plio-Pleistocene denitrification in the eastern tropical North Pacific: Intensification at 2.1 Ma: ETNP denitrification intensification at 2.1 MA. *Geochemistry, Geophysics, Geosystems*, *9*(11), Q11006. https://doi.org/10.1029/2008GC002044

Lo, L., Shen, C.-C., Zeeden, C., Tsai, Y.-H., Yin, Q., Yang, C.-C., et al. (2022). Orbital control on the thermocline structure during the past 568 kyr in the Solomon Sea, southwest equatorial Pacific. *Quaternary Science Reviews*, *295*, 107756. https://doi.org/10.1016/j.quascirev.2022.107756

Lyle, M. W., Drury, A. J., Tian, J., Wilkens, R. H., & Westerhold, T. (2019). *Table SM-14: ODP site 138-849 spliced benthic foraminiferal stable isotope data* (p. 7171 data points) [Text/tab-separated-values]. PANGAEA. https://doi.org/10.1594/PANGAEA.904425

Martin, H., & McMinn, A. (1994). Late Cainozoic vegetation History of North-Western Australia, from the palynology of a deep sea core (ODP Site 765). *Australian Journal of Botany*, *42*(1), 95. https://doi.org/10.1071/BT9940095

Martin, H. A. (2006). Cenozoic climatic change and the development of the arid vegetation in Australia. *Journal of Arid Environments*, *66*(3), 533–563. https://doi.org/10.1016/j.jaridenv.2006.01.009

Martínez-Garcia, A., Rosell-Melé, A., Jaccard, S. L., Geibert, W., Sigman, D. M., & Haug, G. H. (2011). Southern Ocean dust–climate coupling over the past four million years. *Nature*, *476*(7360), 312–315. https://doi.org/10.1038/nature10310

Martínez-Garcia, A., Rosell-Melé, A., McClymont, E. L., Gersonde, R., & Haug, G. H. (2010). Subpolar link to the emergence of the modern equatorial pacific cold tongue. *Science*, *328*(5985), 1550–1553. https://doi.org/10.1126/science.1184480

McLaren, S., Wallace, M. W., & Reynolds, T. (2012). The late Pleistocene evolution of palaeo megalake Bungunnia, southeastern Australia: A sedimentary record of fluctuating lake dynamics, climate change and the formation of the modern Murray River. *Palaeogeography, Palaeoclimatology, Palaeoecology*, *317–318*, 114–127. https://doi.org/10.1016/j.palaeo.2011.12.020

Meyers, P. A. (1994). Preservation of elemental and isotopic source identification of sedimentary organic matter. *Chemical Geology*, *114*(3–4), 289–302. https://doi.org/10.1016/0009-2541(94)90059-0

Mix, A. C., Pisias, N. G., Rugh, W. D., Wilson, J., Morey, A. E., & Hagelberg, T. K. (1995). *Final stable oxygen and carbon isotope ratios of benthic foraminifera versus age of ODP Site 138-849 on the East Pacific Rise* (p. 4245 data points) [Text/tab-separated-values]. PANGAEA. https://doi.org/10.1594/PANGAEA.60261

Müller, A., & Opdyke, B. N. (2000). Glacial-interglacial changes in nutrient utilization and paleoproductivity in the Indonesian Throughflow sensitive Timor Trough, easternmost Indian Ocean. *Paleoceanography*, *15*(1), 85–94. https://doi.org/10.1029/1999PA900046

Müller, P. J., Kirst, G., Ruhland, G., Von Storch, I., & Rosell-Melé, A. (1998). Calibration of the alkenone paleotemperature index U37K′ based on core-tops from the eastern South Atlantic and the global ocean (60°N-60°S). *Geochimica et Cosmochimica Acta*, *62*(10), 1757–1772. https://doi.org/10.1016/S0016-7037(98)00097-0

Paillard, D., Labeyrie, L., & Yiou, P. (1996). Macintosh Program performs time-series analysis. *Eos, Transactions American Geophysical Union*, *77*(39), 379. https://doi.org/10.1029/96EO00259

Pei, R., Kuhnt, W., Holbourn, A., Hingst, J., Koppe, M., Schultz, J., et al. (2021). Monitoring Australian Monsoon variability over the past four glacial cycles. *Palaeogeography, Palaeoclimatology, Palaeoecology*, *568*, 110280. https://doi.org/10.1016/j.palaeo.2021.110280

Peterson, L. C., Lawrence, K. T., Herbert, T. D., Caballero-Gill, R., Wilson, J., Huska, K., et al. (2020). Plio-Pleistocene Hemispheric (A)Symmetries in the Northern and Southern Hemisphere midlatitudes. *Paleoceanography and Paleoclimatology*, *35*(3), e2019PA003720. https://doi.org/10.1029/2019PA003720

Petrick, B., Martínez-García, A., Auer, G., Reuning, L., Auderset, A., Deik, H., et al. (2019). Glacial Indonesian Throughflow weakening across the Mid-Pleistocene climatic transition. *Scientific Reports*, *9*(1), 16995. https://doi.org/10.1038/s41598-019-53382-0

Pisias, N. G., & Moore, T. C. (1981). The evolution of Pleistocene climate: A time series approach. *Earth and Planetary Science Letters*, *52*(2), 450–458. https://doi.org/10.1016/0012-821X(81)90197-7

Prahl, F. G., & Wakeham, S. G. (1987). Calibration of unsaturation patterns in long-chain ketone compositions for palaeotemperature assessment. *Nature*, *330*(6146), 367–369. https://doi.org/10.1038/330367a0

Rafter, P. A., & Charles, C. D. (2012). Pleistocene equatorial Pacific dynamics inferred from the zonal asymmetry in sedimentary nitrogen isotopes: Currents. *Paleoceanography*, *27*(3), PA3102. https://doi.org/10.1029/2012PA002367

Ravelo, A. C., Andreasen, D. H., Lyle, M., Olivarez Lyle, A., & Wara, M. W. (2004). Regional climate shifts caused by gradual global cooling in the Pliocene epoch. *Nature*, *429*(6989), 263–267. https://doi.org/10.1038/nature02567

Ravelo, A. C., Simonne Dekens, P., & McCarthy, M. (2006). Evidence for El Niño–like conditions during the Pliocene. *Geological Society of America Today*, *16*(3), 4. https://doi.org/10.1130/1052-5173(2006)016<4:EFENLC>2.0.CO;2

Rein, B., & Sirocko, F. (2002). In-situ reflectance spectroscopy—Analysing techniques for high-resolution pigment logging in sediment cores. *International Journal of Earth Sciences*, *91*(5), 950–954. https://doi.org/10.1007/s00531-002-0264-0

Rohling, E. J., Foster, G. L., Grant, K. M., Marino, G., Roberts, A. P., Tamisiea, M. E., & Williams, F. (2014). Sea-level and deep-sea-temperature variability over the past 5.3 million years. *Nature*, *508*(7497), 477–482. https://doi.org/10.1038/nature13230

Rosenthal, Y., Holbourn, A. E., Kulhanek, D. K., & Expedition 363 Scientists (2017). *International ocean discovery program expedition 363 preliminary report western pacific warm pool neogene and quaternary records of Western Pacific warm pool paleoceanography*. International Ocean Discovery Program. https://doi.org/10.14379/iodp.pr.363.2017

Rosenthal, Y., Holbourn, A. E., Kulhanek, D. K., & Expedition 363 Scientists (2018). In *Western pacific warm pool* (Vol. 363). International Ocean Discovery Program. https://doi.org/10.14379/iodp.proc.363.2018

Rousselle, G., Beltran, C., Sicre, M.-A., Raffi, I., & De Rafélis, M. (2013). Changes in sea-surface conditions in the Equatorial Pacific during the middle Miocene–Pliocene as inferred from coccolith geochemistry. *Earth and Planetary Science Letters*, *361*, 412–421. https://doi.org/10.1016/j.epsl.2012.11.003

Schlitzer, R. (2023). Ocean data view. Retrieved from odv.awi.de

Schouten, S., Hopmans, E. C., Schefuß, E., & Sinninghe Damsté, J. S. (2002). Distributional variations in marine crenarchaeotal membrane lipids: A new tool for reconstructing ancient sea water temperatures? *Earth and Planetary Science Letters*, *204*(1–2), 265–274. https://doi.org/10.1016/S0012-821X(02)00979-2

Singarayer, J. S., Valdes, P. J., & Roberts, W. H. G. (2017). Ocean dominated expansion and contraction of the late Quaternary tropical rainbelt. *Scientific Reports*, *7*(1), 9382. https://doi.org/10.1038/s41598-017-09816-8

Smith, R. A., Castañeda, I. S., Groeneveld, J., De Vleeschouwer, D., Henderiks, J., Christensen, B. A., et al. (2020). Indonesian throughflow and Leeuwin current dynamics in the Plio-Pleistocene. 2020. PP037-0005.

Stuut, J.-B. W., Temmesfeld, F., & De Deckker, P. (2014). A 550 ka record of Aeolian activity near North West Cape, Australia: Inferences from grain-size distributions and bulk chemistry of SE Indian Ocean deep-sea sediments. *Quaternary Science Reviews*, *83*, 83–94. https://doi.org/10.1016/j.quascirev.2013.11.003

Stuut, J. W., De Deckker, P., Saavedra-Pellitero, M., Bassinot, F., Drury, A. J., Walczak, M. H., et al. (2019). A 5.3-million-year history of monsoonal precipitation in northwestern Australia. *Geophysical Research Letters*, *46*(12), 6946–6954. https://doi.org/10.1029/2019GL083035

Sun, Y., Clemens, S. C., An, Z., & Yu, Z. (2006). Astronomical timescale and palaeoclimatic implication of stacked 3.6-Myr monsoon records from the Chinese Loess Plateau. *Quaternary Science Reviews*, *25*(1–2), 33–48. https://doi.org/10.1016/j.quascirev.2005.07.005

Sun, Y., Yin, Q., Crucifix, M., Clemens, S. C., Araya-Melo, P., Liu, W., et al. (2019). Diverse manifestations of the mid-Pleistocene climate transition. *Nature Communications*, *10*(1), 352. https://doi.org/10.1038/s41467-018-08257-9

Suppiah, R. (1992). The Australian summer monsoon: A review. *Progress in Physical Geography: Earth and Environment*, *16*(3), 283–318. https://doi.org/10.1177/030913339201600302

Susanto, R. D., Gordon, A. L., & Zheng, Q. (2001). Upwelling along the coasts of Java and Sumatra and its relation to ENSO. *Geophysical Research Letters*, *28*(8), 1599–1602. https://doi.org/10.1029/2000GL011844

Talley, L. D., & Sprintall, J. (2005). Deep expression of the Indonesian throughflow: Indonesian intermediate water in the south equatorial current. *Journal of Geophysical Research*, *110*(C10), C10009. https://doi.org/10.1029/2004JC002826

Tomczak, M., & Godfrey, J. S. (1994). *Regional oceanography: An introduction* (1st ed.). Pergamon.

Tomczak, M., & Godfrey, J. S. (2003). *Regional oceanography: An introduction* (2. ed). Daya Publ. House.

Wang, P., Clemens, S., Beaufort, L., Braconnot, P., Ganssen, G., Jian, Z., et al. (2005). Evolution and variability of the Asian monsoon system: State of the art and outstanding issues. *Quaternary Science Reviews*, *24*(5–6), 595–629. https://doi.org/10.1016/j.quascirev.2004.10.002

Wang, P., Tian, J., & Lourens, L. J. (2010). Obscuring of long eccentricity cyclicity in Pleistocene oceanic carbon isotope records. *Earth and Planetary Science Letters*, *290*(3–4), 319–330. https://doi.org/10.1016/j.epsl.2009.12.028

Wara, M. W., Ravelo, A. C., & Delaney, M. L. (2005). Permanent El Niño-like conditions during the Pliocene warm period. *Science*, *309*(5735), 758–761. https://doi.org/10.1126/science.1112596

White, S. M., & Ravelo, A. C. (2020). The benthic B/Ca record at site 806: New constraints on the temperature of the West Pacific warm pool and the "El Padre" State in the Pliocene. *Paleoceanography and Paleoclimatology*, *35*(10), e2019PA003812. https://doi.org/10.1029/2019PA003812

Xin, S., Shen, J., Zhang, W., Sun, W., & Xiao, X. (2020). East Asian winter monsoon evolution since the late Pliocene based on a pollen record from Lake Xingkai, northeast Asia. *Quaternary Research*, *93*, 40–59. https://doi.org/10.1017/qua.2019.45

Zhang, P., Xu, J., Holbourn, A., Kuhnt, W., Beil, S., Li, T., et al. (2020). Indo-pacific Hydroclimate in response to changes of the intertropical convergence zone: Discrepancy on precession and obliquity bands over the last 410 kyr. *Journal of Geophysical Research: Atmospheres*, *125*(14), e2019JD032125. https://doi.org/10.1029/2019JD032125

Zhang, Y., Andrade, T., Ravelo, A. C., Gong, L., Holbourn, A., Connock, G., et al. (2023). NOAA/WDS Paleoclimatology - Site U1483 (Timor Sea) terrigenous input and productivity data over the last 2 Myrs [Dataset]. NOAA National Centers for Environmental Information. https://doi.org/10.25921/dz26-9c85

References From the Supporting Information

Li, M., Hinnov, L., & Kump, L. (2019). Acycle: Time-series analysis software for paleoclimate research and education. *Computers & Geosciences*, *127*, 12–22. https://doi.org/10.1016/j.cageo.2019.02.011

Torrence, C., & Compo, G. P. (1998). A practical guide to wavelet analysis. *Bulletin of the American Meteorological Society*, *79*(1), 61–78. https://doi.org/10.1175/1520-0477(1998)079<0061:APGTWA>2.0.CO;2